

# Crustal structure of the central Sunda margin at the onset of oblique subduction

Heidrun Kopp,<sup>1</sup> Ernst R. Flueh,<sup>1</sup> Dirk Klaeschen,<sup>1</sup> Jörg Bialas<sup>1</sup> and Christian Reichert<sup>2</sup>

<sup>1</sup>GEOMAR Research Center for Marine Geosciences, Wischhofstrasse 1–3, 24148 Kiel, Germany. E-mail: hkopp@geomar.de

<sup>2</sup>BGR Federal Institute for Geosciences and Natural Resources, Hannover, Germany

Accepted 2001 June 15. Received 2001 June 13; in original form 2001 April 10

## SUMMARY

The convergent margin of the central Sunda Arc in Indonesia was the target of a reflection and refraction seismic survey conducted in 1998 and 1999. Along two seismic lines across the subduction complex off southern Sumatra and off Sunda Strait, coincident multichannel and wide-angle data were collected, complemented by two refraction strike-lines in the forearc basin off Sumatra. The combined analysis of the acquired data allows us to present a detailed model of the subduction zone where initiation of strain partitioning occurs due to the onset of oblique subduction. The dip of the subducted plate is well defined along both dip-lines and a lateral increase from 5° to 7° from beneath the outer high off Sumatra to Sunda Strait is supported by complementary gravity modelling. The downgoing slab is traced to a depth of more than 30 km. On both reflection dip-lines, a clearly developed backstop structure underlying a trench slope break defines the landward termination of the active accretionary prism and separates it from the outer high. Active subduction accretion is supported by laterally increasing velocities between the deformation front and the active backstop structure. Seismic velocities of the outer high are moderate along both lines ( $< 5.8 \text{ km s}^{-1}$  at 20 km depth), suggesting a sedimentary composition. Reduced reflectivity beneath a rugged top basement traced along the outer high of both dip-lines supports a high degree of deformation and material compaction. Several kilometres of sediment has accumulated in the forearc domain, although a distinct morphological basin is only recognized off southern Sumatra and is not developed off Sunda Strait. The bathymetric elevation of the Java shelf that is encountered in the southern Sunda Strait corresponds to increased velocities of a basement high there and is connected to extensional structures of the Sunda Strait transtensional basin. Differences observed in the morphology of the forearc domain are also reflected in the lower crustal structure. Off southern Sumatra, the velocity–depth model clearly indicates a continental-type crust underlying the forearc basin, whereas lower velocities are found beneath the Sunda Strait forearc domain. Off Sumatra, some 3-D constraint on the upper plate structure is gained from the refraction strike-lines, which in addition is supported by synthetic data modelling.

**Key words:** active margin, crustal structure, seismic reflection, seismic refraction, subduction, Sunda Arc.

## 1 INTRODUCTION

The central Sunda margin along the southern projection of the Indonesian Archipelago (Fig. 1) represents a prime target for investigations of the variation of forearc structures related to an increasing obliquity of plate collision. The curvature of the trench is the main characteristic of this subduction complex, resulting in regimes of frontal subduction off Java to oblique

subduction off Sumatra that becomes subparallel towards the Andaman Sea (Fig. 1) (Fitch 1972; Hamilton 1979; Moore *et al.* 1980; Huchon & Le Pichon 1984). The region provides an archetypal example of the partitioning of convergent motion into a component of thrusting at the trench and a component of arc-parallel strike-slip motion. This results in a lateral displacement of the forearc platelet along the dextral Sumatra strike-slip fault and possibly along the Mentawai fault zone,

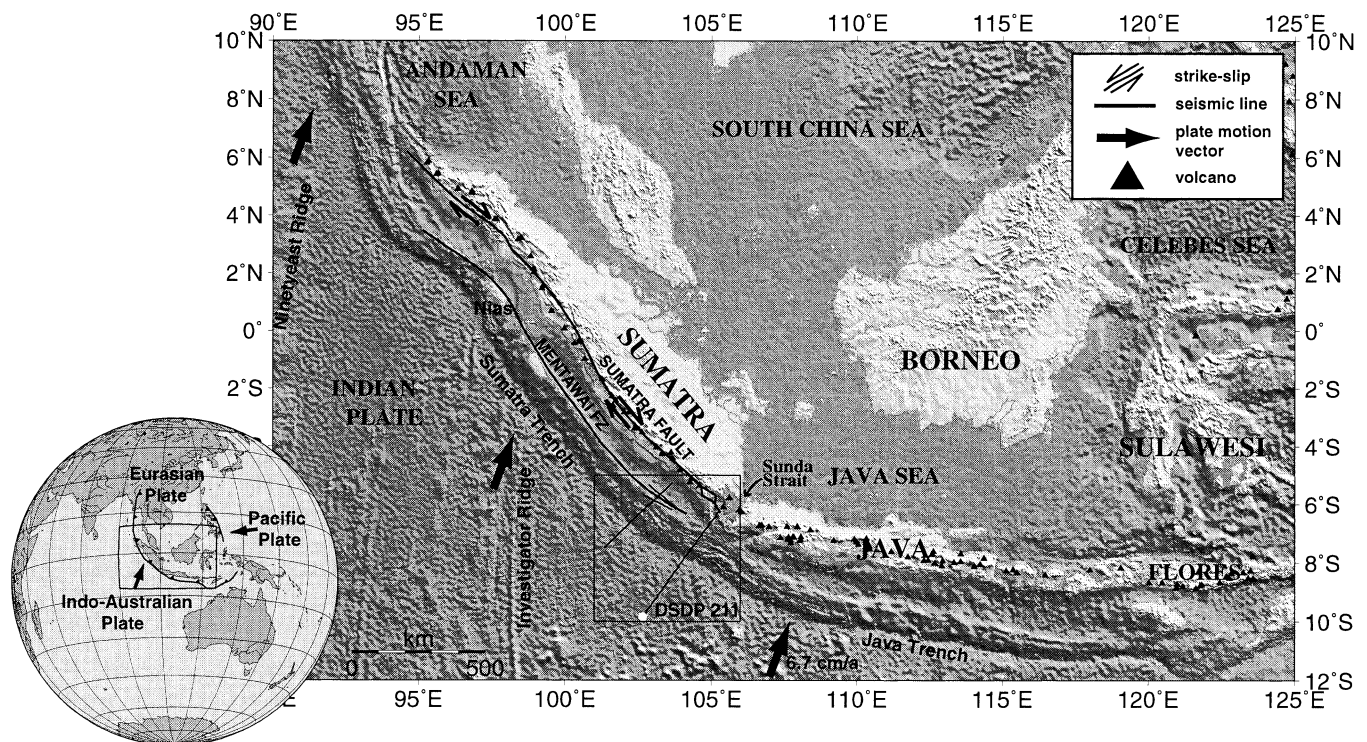


**Figure 1.** Bathymetric map of western Indonesia where the Indo-Australian plate is thrust beneath Eurasia along the Sumatra and Java trench system. The change in orientation of the Sunda margin causes an increase in subduction obliquity to the northwest, where strain partitioning leads to the initiation of the Sumatra strike-slip fault and possibly the Mentawai transpressional fault. The study area is indicated by the box (see Fig. 2). Plate motion vectors are from the Australia–Eurasia rotation pole after DeMets *et al.* 1990). Volcano distribution is taken from the Smithsonian Global Volcanism Program (online data set at <http://www.mnh.si.edu/gvp/volcano/region06/index.htm>). Bathymetric information is extracted from the Topex data set (Sandwell & Smith 1997).

which runs along the outer border of the forearc basin (Diamant *et al.* 1992; Malod & Kemal 1996). The increasing obliquity in the Sumatra area induces decoupling of the downgoing slab from the upper plate by strain partitioning (Malod & Kemal 1996). As can be deduced from the analysis of slip vectors, decoupling off Sumatra is not fully complete (McCaffrey 1991, 1992, 1996). Geodetic observations show a high degree of coupling of the forearc domain with the downgoing slab in the south, decreasing to the north (Prawirodirdjo *et al.* 1997). Thus decoupling by strain partitioning alone cannot fully explain the difference in the amount of extension in the Sunda Strait (<100 km) and the Andaman Sea (>400 km) (Bellier & Sébrier 1995; McCaffrey 1996). Additional stretching of the forearc domain could account for this discrepancy and is compatible with an increase in slip rate along the Sumatra fault (Bellier & Sébrier 1995). Neither the mechanism of the forearc stretching nor the role of the Mentawai fault zone is yet fully understood. The tectonic differences and dynamics along the 5600 km long Sunda Arc also result from the variation of several other geological parameters, including the age of the subducted plate and the thickness of the incoming sediment cover (Curry *et al.* 1977; Hamilton 1979; Moore *et al.* 1980).

The Sunda margin has been the locus for a series of scientific investigations (McCaffrey 1992; Izart *et al.* 1994; Malod & Kemal 1996; Samuel & Harbury 1996). However, only scarce seismic data cover the transition zone from oblique to frontal subduction off southern Sumatra and the Sunda Strait (Fig. 1). A detailed investigation of this progression was the aim of project GINCO (geoscientific investigations along the active

convergence zone between the eastern Eurasian and Indo-Australian plates off Indonesia), during which we collected multichannel seismic reflection (MCS) and wide-angle reflection–refraction data across the Sunda subduction zone and within the forearc domain using the RV *Sonne* from November 1998 to January 1999. We present here the interpretation of two seismic lines off southern Sumatra and off Sunda Strait, along which coincident MCS and wide-angle seismic data were acquired. In addition, we discuss two wide-angle strike-lines covering the forearc domain off Sumatra. These strike-lines yield some 3-D constraint on the velocity–depth model derived. Along the two wide-angle dip-lines the downgoing plate is tracked from the trench to a depth of more than 30 km, which is supported by supplementary gravity modelling. The velocity structure of the forearc domain is derived from forward ray tracing of the two strike-lines, complemented by comparisons with synthetic data. Moreover, the structure of the Sunda margin is resolved in considerable detail by the MCS data. Based on these newly acquired seismic data and their interpretation we present a detailed cross-section and discuss the crustal structure of the subduction zone off southern Sumatra and Sunda Strait.

## 2 GEODYNAMIC SETTING

The Sunda Arc marks the collision zone where the Indo-Australian Plate is thrust beneath the Eurasian Plate (Fig. 1). The subduction system has been active since at least the Oligocene and evolved after the late Eocene collision of India with Eurasia (Hamilton 1988). The present-day kinematics of

the Sunda margin (Fig. 1) are described to first order by global plate motion solutions (NUVEL-1 and NUVEL-1 A) (DeMets *et al.* 1990, 1994). Additional GPS measurements determine the motion of Australia with respect to West Java at  $67 \text{ mm yr}^{-1}$  in a  $\text{N}11^\circ\text{E}$  direction, which is orthogonal to the trench (Tregoning *et al.* 1994).

The investigated area is positioned across the Sunda collision zone off southern Sumatra and off Sunda Strait (Fig. 2). Located at the point of directional change of the trench, the Sunda Strait marks a transition zone between orthogonal subduction off Java and oblique subduction off Sumatra. The Sunda Strait is located at the southern termination of the Sumatra fault (Malod *et al.* 1995) and has evolved under a transtensional regime, as is evident from seismic investigations (Diamant *et al.* 1990; Lelgemann *et al.* 2000) and from local seismicity (Harjono 1991). The age of the incoming plate increases from Sumatra in the west to Flores in the east (Fig. 1). Off southern Sumatra, the plate age is about 90 Myr (Widiyantoro & van der Hilst 1996). The increase in age is consistent with an increase in plate dip along the arc (Widiyantoro & van der Hilst 1996) and an

increasing depth of seismic activity. Beneath the Sumatran part of the arc, seismicity does not exceed 250 km in depth (Puspito & Shimazaki 1995), while further east seismic activity down to 670 km depth occurs. The width and elevation of the accretionary complex and outer high increase to the north of Sumatra (Moore *et al.* 1980), where sediment influx on the incoming plate is greater than off Java. Parts of the outer high are exposed subaerially in an island chain (e.g. Pulau Enggano in Fig. 2) that parallels the Sumatra trench (Moore *et al.* 1980). The island of Nias (Fig. 1) provided the focus for a number of geophysical and geological investigations. Early studies (Moore *et al.* 1980) interpreted Nias as part of the subduction complex that had been uplifted due to the accretion of thick Bengal fan sediments that reached the area in the Middle to Late Miocene. More recently, Samuel *et al.* (1995) interpreted Nias as the result of the inversion of extensional sub-basins. Early refraction studies around Nias (Kieckhefer *et al.* 1980) covered the wedge and outer high of about 20 km thickness that make up Nias island. Velocities are moderate ( $< 5 \text{ km s}^{-1}$ ), increasing towards the forearc basin. The nature of the forearc

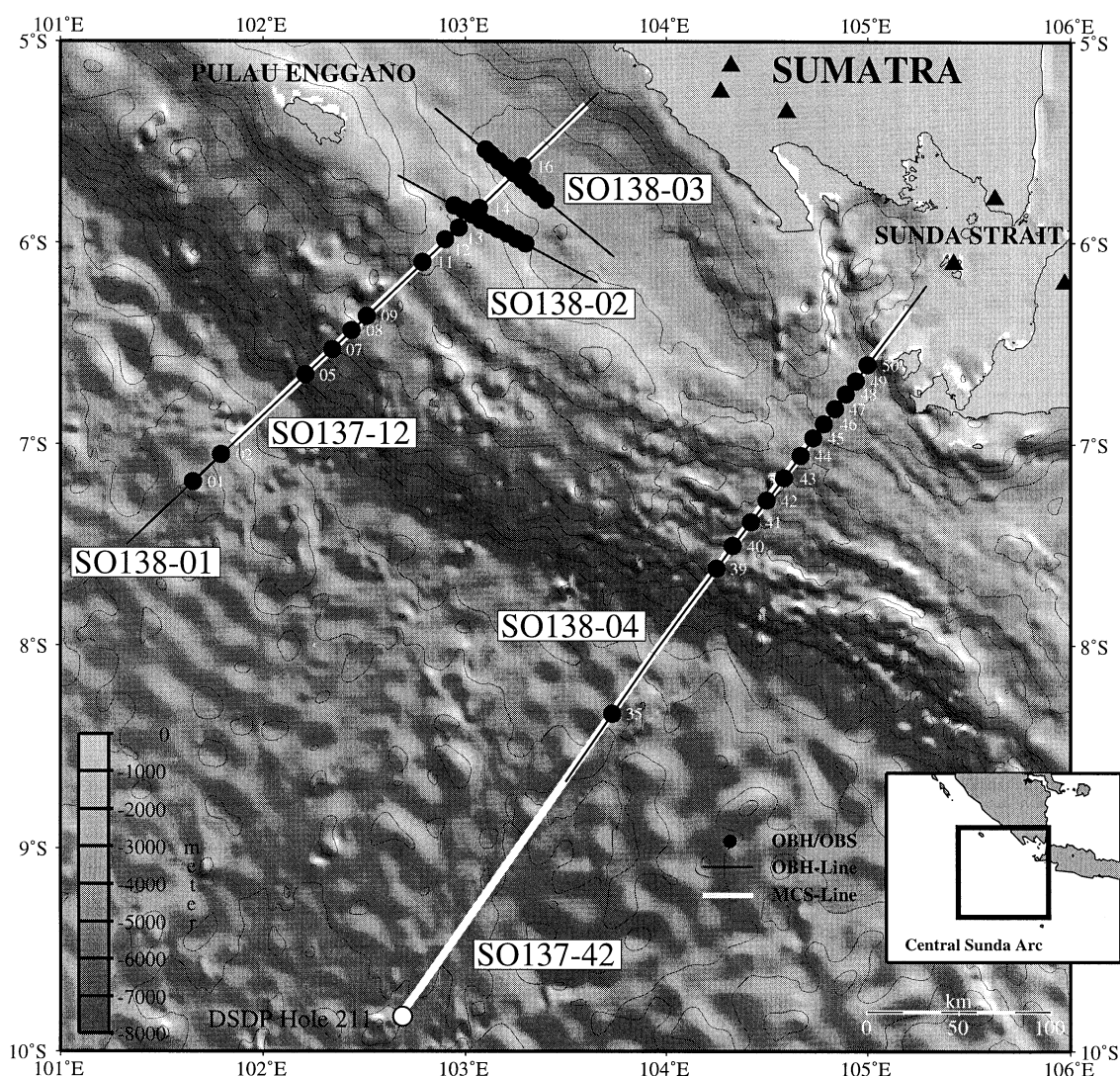


**Figure 2.** Location map of the seismic survey with seafloor bathymetry illuminated from the northeast. A total of 50 instruments recorded wide-angle data along profiles totalling a length of 950 km. Refraction and reflection seismic data were acquired along dip-lines SO138-01 (SO137-12) and SO138-04 (SO137-42). Shooting along SO137-42 was extended into the ocean basin. Additional wide-angle data were recorded along the two strike-lines SO138-02 and SO138-03. Black triangles mark volcano positions.

basin basement is assumed to be continental. Off Sumatra, a distinct forearc basin is divided into several large sub-basins (Moore *et al.* 1980). The seismic stratigraphy of the forearc domain has been determined around Nias from reflection seismic data and borehole information (Beaudry & Moore 1981, 1985; Izart *et al.* 1994). Expanding the work of Beaudry & Moore (1981, 1985), Izart *et al.* (1994) proposed Palaeogene uplift of the Sumatra margin followed by Miocene subsidence that increased during the Pliocene and Quaternary.

### 3 SEISMIC DATA

Multichannel seismic reflection data were collected during the German RV *Sonne* cruise SO137 (Reichert *et al.* 1999). Profile SO137-12 is located off southern Sumatra, approximately 75 km southeast of the island of Enggano (Fig. 2) and extends SW–NE from the Sunda trench to the Sumatra shelf. A second line (SO137-42) covers the subduction complex further south-east off Sunda Strait and extends about 250 km seawards of the trench into the ocean basin. The data were recorded using a 3 km long streamer with a maximum of 120 channels and a recording time of 14 s. Along both lines coincident wide-angle data were acquired (profiles SO138-01 and SO138-04 in Fig. 2) during the RV *Sonne* cruise SO138 (Flueh *et al.* 1999). Both ocean bottom hydrophone (OBH) lines extend about 100 km seawards of the trench to obtain reversed coverage of the oceanic crust. In addition, two wide-angle strike-lines were shot across OBH profile 01. Profile 02 covers the landward part of the outer high at the transition to the forearc basin, while line 03 runs along the strike of the depocentre of the forearc basin. Along the various profiles a total of 50 stations were deployed, consisting mainly of GEOMAR OBHs (Flueh & Bialas 1996), with a few ocean bottom seismometers (OBSs). Instrument locations are given in Fig. 2. The same seismic source was applied during both cruises and signals were generated by a tuned set of 20 airguns grouped in two identical linear subarrays. The total volume of the array is 51.2 l (3.124 cu in). For the multichannel reflection recordings a shot interval of 50 m and a hydrophone spacing of 25 m were chosen, resulting in a common midpoint (CMP) distance of 12.5 m and a maximum fold of 30. Processing included frequency filtering after amplitude balancing and trace editing of the shot gathers. A primary focus during data processing was multiple removal, which was performed in the frequency–wavenumber ( $f$ – $k$ ) domain enabled by move-out differences between primary and multiple events in the CMP gather. A trace interpolation was applied to prevent aliasing before  $f$ – $k$  multiple reduction. An enhanced signal resolution and further multiple suppression were achieved by a two-gated predictive deconvolution. However, the demultiple process is inhibited due to limited energy coherence within the CMP gathers resulting from the highly variable seafloor topography. Multiple energy still remains, especially beneath the outer high, where significant seafloor depth variations occur (e.g. Fig. 3a). A post-stack time migration is included in the processing sequence. A smoothed velocity field derived from the wide-angle data modelling served as a starting model for the migration process.

For the wide-angle data recording, shots were triggered at time intervals of 60 s at a speed of 5.5 knots, resulting in an average shotpoint distance of 167 m. Wide-angle data processing included relocation of the instrument position by analysing the direct arrivals followed by a low-cut frequency filter. A two-

gated predictive deconvolution was applied to the data to improve the temporal resolution. A time- and offset-dependent filtering was chosen to account for the broad frequency range contained in the data as well as the significant seafloor depth variation. The seismic energy was sufficient to trace signals on the record sections over distances of 60–80 km, and data quality is good on average. Only selected record sections are shown.

Fig. 3(a) displays the southwestern part of MCS line SO137-12, covering the trench and deformation front, which exhibit a water depth of approximately 6750 m. The topography between the deformation front and an active backstop structure that was recognized around CDP 25 500 displays several distinct ridges and troughs in which small amounts of recent sediment are trapped. Landwards, a rough basement top (Fig. 3b) becomes visible, beneath which little internal structure is resolved. Here the data are further obscured by remnants of the seafloor multiple. Fig. 3(c) shows the landwardmost part of the profile from the northeastern part of the outer high to the Sumatra shelf. In the forearc basin the thick sediment infill is well resolved as it overlaps the Sumatra shelf above the high-amplitude basement top.

Fig. 4(a) displays the southern part of profile SO137-42, with only the first 40 km seaward of the trench shown. Landward of the trench a number of ridges above the top of the downgoing plate are present between the deformation front and a slope break that defines the active backstop structure (CDP 24 600). The upper segments of the outer high are disturbed by a number of faults, creating a ridge and trough morphology (Fig. 4b). A distinct forearc basin, as seen in profile 12 (Fig. 3c), is absent on this line. The sedimentary units thicken towards the Java shelf (Fig. 4c) and gain a similar thickness of more than 4 km to that of line 12.

#### 3.1 Modelling

An integrative approach using both the wide-angle and the near-vertical-incidence reflection data was chosen to reveal the deeper structure along the transects. The two data sets were acquired during two consecutive cruises to meet the different demands concerning the shot intervals for wide-angle and multichannel recordings.

A 2-D forward modelling technique (Luetgert 1992) using a top-to-bottom approach was applied to derive the velocity–depth models (Figs 5 and 6), using both first and later arrivals. Phase nomenclature is given in Table 1. The MCS data helped to model the upper segments of the dip-lines (Fig. 7). The two strike-lines P02 and P03 (see Fig. 2) were later tied to the dip-line SO138-01 and thus further constrained the velocity field along the Sumatra transect. Uncertainties in identifying first arrivals from refracted waves through the upper sections of the outer high and forearc domain and from refracted waves through the oceanic crust ranged from less than  $\pm 50$  ms for arrivals in the near-offset range ( $< 30$  km) to about  $\pm 100$  ms at larger offsets due to a poorer signal-to-noise ratio.  $P_mP$  reflections are present at a number of stations on the outer high and ocean basin as well as in the forearc domain on profile 04. Due to their late arrival times these events could only be picked with accuracies of less than  $\pm 100$  ms (e.g. OBHs 01 and 05 in Fig. 8). Both dip-lines (01 and 04) show a fairly complex velocity field reflecting the rapid change in water depth and the variable composition and compaction of the accretionary complex and



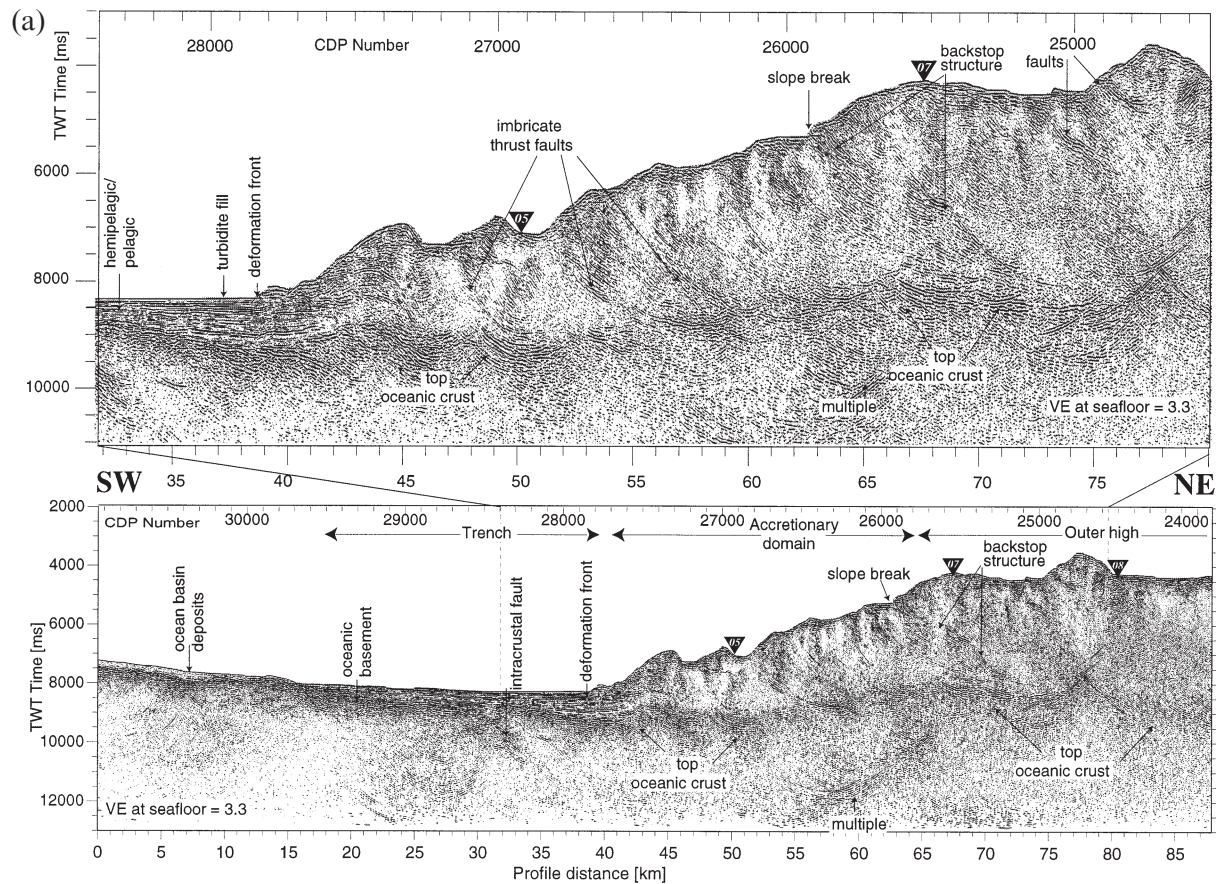


**Figure 3.** (a) Seaward portion of MCS profile SO137-12 off southern Sumatra. The active accretionary domain extends from the trench to the slope break marking the backstop structure between CDPs 25 000 and 26 000. The accretionary prism is characterized by intense faulting leading to a chaotic seismic signature. The top of the subducted plate can be followed from the trench to beneath the outer high (b). The subducting oceanic crust is cut by several large landward-dipping faults. The corresponding velocity–depth model (Fig. 5) shows laterally increasing velocities in the accretionary domain. Black triangles mark deployed wide-angle stations. (b) Central part of MCS line SO137-12 across the outer high and the seaward forearc sub-basin. The rough basement top inhibits reflectivity within the outer high. Tectonic activity is evident in several faults across the outer high. The top of the subducted plate can be traced to around profile km 120. Black triangles mark deployed wide-angle stations. (c) Landward part of MCS line SO137-12 covering the forearc basin, which shows a maximum of 5 km of sediment fill. The Mentawai fault zone represents a major structural break, separating a smaller sub-basin (CDPs 16 900–18 700) carrying about 3 km of sediment from the main basin. Elevation in seafloor depth across the fault zone is about 600 m. Black triangles mark deployed wide-angle stations.

the outer high (Figs 5 and 6). The position of the basement top, which is present along both dip-lines, as well as the depth of the basement beneath the forearc domain and the top of the subducted plate were identified from the MCS data and are also prominent wide-angle reflections. A comparison of the main

reflection horizons with major velocity changes of the final wide-angle models along the two profiles is shown in Fig. 7. During modelling, the main horizons identified in the MCS data were incorporated by simulation of an ‘exploding reflector’, where the velocity discontinuities are modelled as the source depth for zero-offset ray paths travelling upwards to be recorded at the sea surface. These one-way ray paths thus simulate the reflected waves.

**Table 1.** Phase nomenclature for wide-angle arrivals.

Phase	Description
$P_{\text{sed1}}, P_{\text{sed2}}$	sedimentary phases
$P_{\text{lac}}$	refraction through lower accretionary complex
$P_{\text{oc}}$	refraction through oceanic crust
$P_{\text{toc}}$	reflection from top of oceanic crust
$P_{\text{up}}$	refraction through upper plate
$P_{\text{up}P}$	reflection from upper plate/lower plate boundary
$P_{\text{m}P}$	reflection from crust–mantle boundary
$P_{\text{n}}$	mantle refraction

## 4 INTERPRETATION

### 4.1 Sumatra transect

The 360 km long OBH profile 01 crosses the trench and accretionary domain as well as the outer high and the southernmost Sumatra forearc sub-basin. A prominent feature traversed by this line is the Mentawai fault zone, which borders the seaward part of the forearc basin and lies between the two strike-lines (Fig. 2).



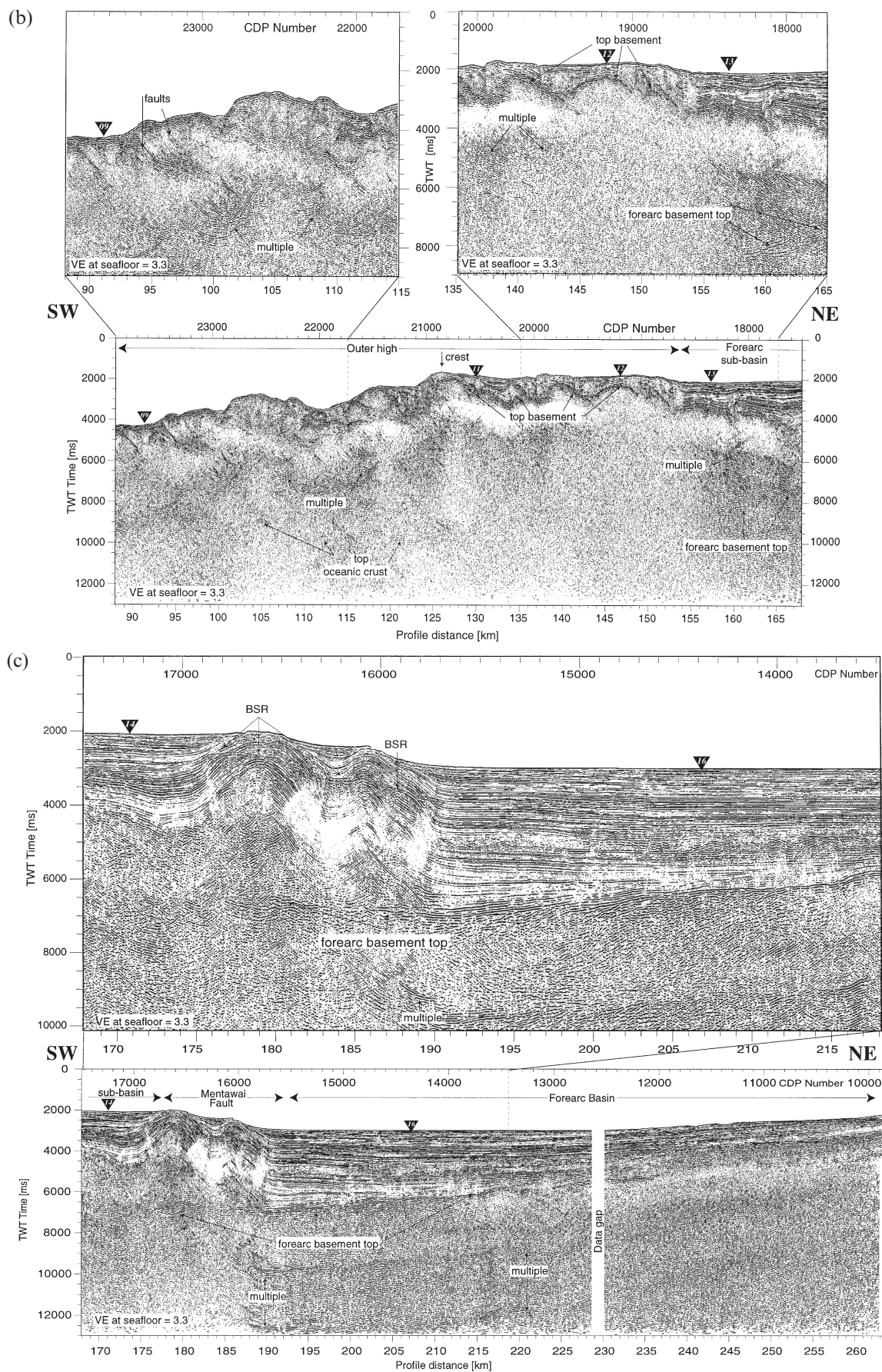
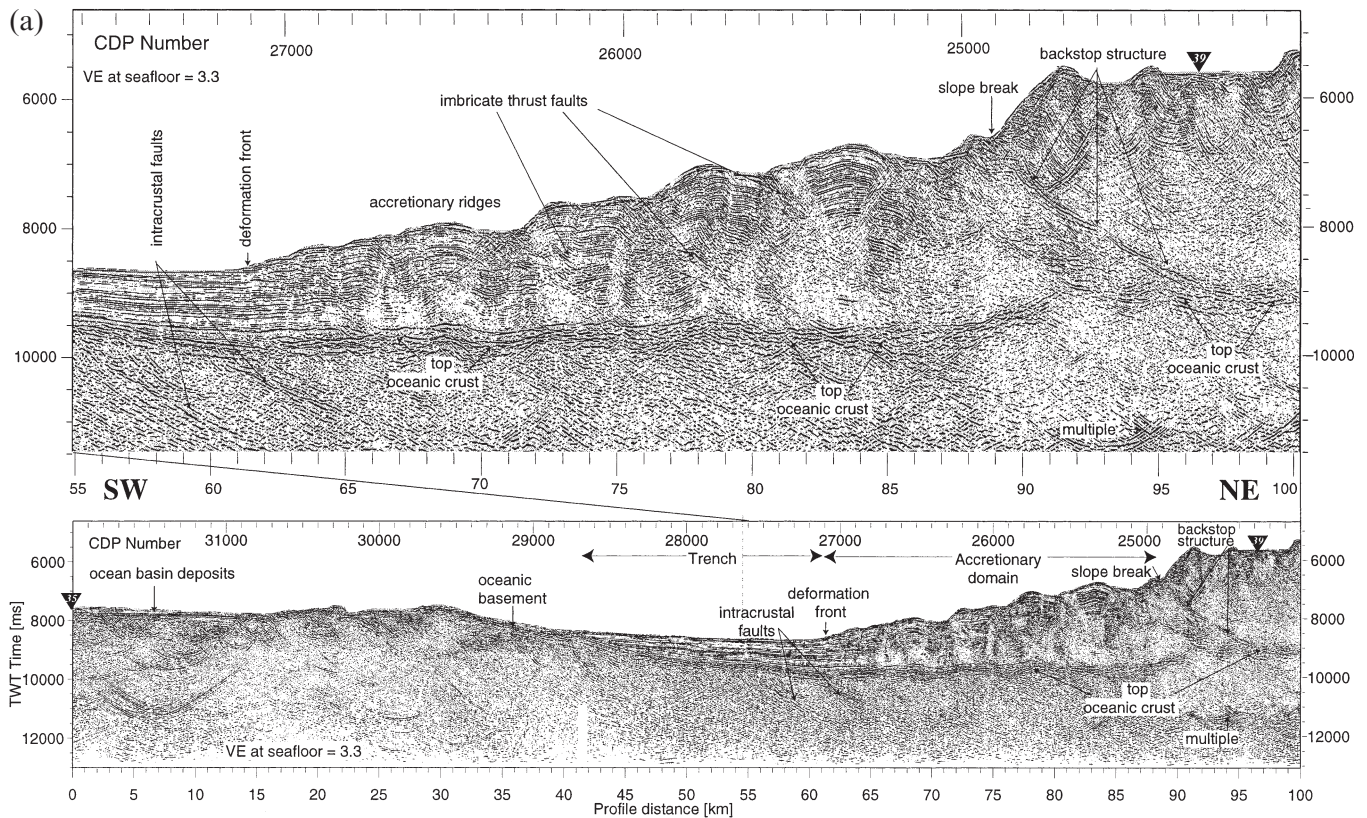


Figure 3. (Continued.)





**Figure 4.** (a) Part of MCS line SO137-42 covering the trench and active accretionary domain. Whereas the seaward portion of the profile extends 250 km onto the ocean basin, only 35 profile kilometres located seaward of the trench is displayed here. The accretionary prism is bounded by the deformation front and the active backstop structure. The downthrusting plate can be followed over 100 km landwards of the deformation front. Several accretionary ridges are recognized on top of the subducted oceanic crust, bounded by imbricate thrust faults. Landward-dipping intracrustal faults are found beneath the trench (CDPs 26 800–27 600). Black triangles mark deployed wide-angle stations. (b) Central part of MCS line SO137-42 across the outer high, beneath which the top of the subducted plate is recognized. A top basement is identified landwards of CDP 21 300. Active faulting still characterizes this part of the subduction complex. The outer high region is not as well expressed as on profile SO137-12 off southern Sumatra. The corresponding velocity–depth model (Fig. 6) shows laterally constant seismic velocities of moderate values. Black triangles mark deployed wide-angle stations. (c) Northeastern part of profile MCS SO137-42 covering the forearc domain and the southern entrance to the Sunda Strait. Tectonic activity mainly affects the older sediments; the younger strata are less disturbed. The onset of the Java shelf around CDP 13 000 is marked by a steep seafloor elevation showing only a thin sedimentary cover seawards of a sedimentary basin (CDPs 10 000–11 500) located within the Sunda Strait. The basement ridge is characterized by high seismic velocities (Fig. 6). Black triangles mark deployed wide-angle stations.

Ocean basin deposits > 500 m thick are visible on the oceanic crust for the first 20 km seaward of the trench, as determined from the time-converted velocity–depth model shown in Fig. 7. The oceanic basement shows some topography, which in parts has not been fully smoothed by the sedimentary cover (e.g. around CDP 29 800 in Fig. 3a). Two instruments (OBHs 01 and OBH 02) were deployed seawards of the trench. These instruments recorded a 2 km thick upper crust, displaying velocities increasing with depth from 4.8 to 6.3 km s<sup>-1</sup>. Phases  $P_{oc}$  record a locally thickened lower crust with velocities increasing from 6.4 to 7.2 km s<sup>-1</sup>. The highly variable Moho depth is imaged in the clear  $P_mP$  and  $P_n$  phases recorded by stations 01 and 05 (Fig. 8). As the shooting terminated 30 km seawards of the trench, the extent of crustal thickening is not well constrained. Mantle velocities of 8.0 km s<sup>-1</sup> beneath the ocean basin are determined by reversed  $P_n$  observations. Several landward-dipping faults in the oceanic basement are visible beneath the sediment cover (Fig. 3a). Some of these faults cut deep into the oceanic crust (CDP 28 400). The trench fill, up to 1.1 km thick, consists of turbiditic sequences above pelagic/

hemipelagic sediment infill. The trench infill is characterized by near-parallel, subhorizontal and landward-divergent facies that overlap the basement.

The top of the oceanic plate can be traced as a strong reflection in the MCS data 80 km landwards of the deformation front beneath the active accretionary domain and parts of the outer high. The reflection displays a high lateral coherence (Figs 3a and b) but is somewhat blurred further landwards by remnants of the seafloor multiple. Several OBH stations deployed on the active accretionary domain and outer high (OBH 05–09) record the top of the oceanic plate as it is thrust beneath the upper plate. OBH 05 (Fig. 8) covers the accretionary domain as well as the trench and parts of the oceanic basin and recorded phase  $P_{loc}$  from the top of the subducted plate beneath the accretionary prism. The high apparent velocities of the  $P_mP$  and  $P_n$  phases at southwestern offsets greater than 25 km are caused by the Moho undulations observed seawards of the trench. Station 07 (Fig. 9) recorded a strong vertical reflection,  $P_{loc}$ , beneath the outer high at 0–9 km offset and a  $P_{oc}$  refraction at greater offsets. Beneath the trench



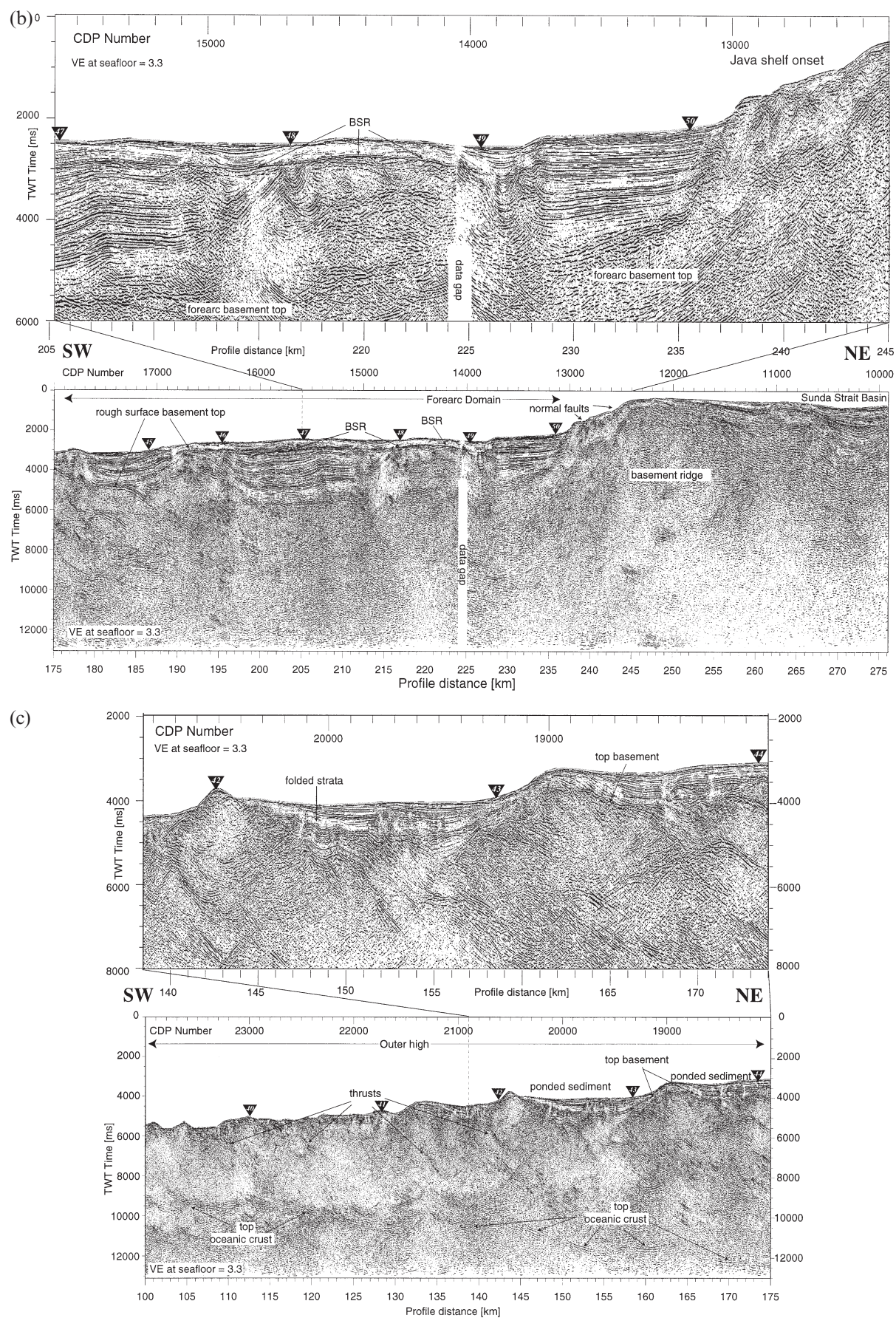
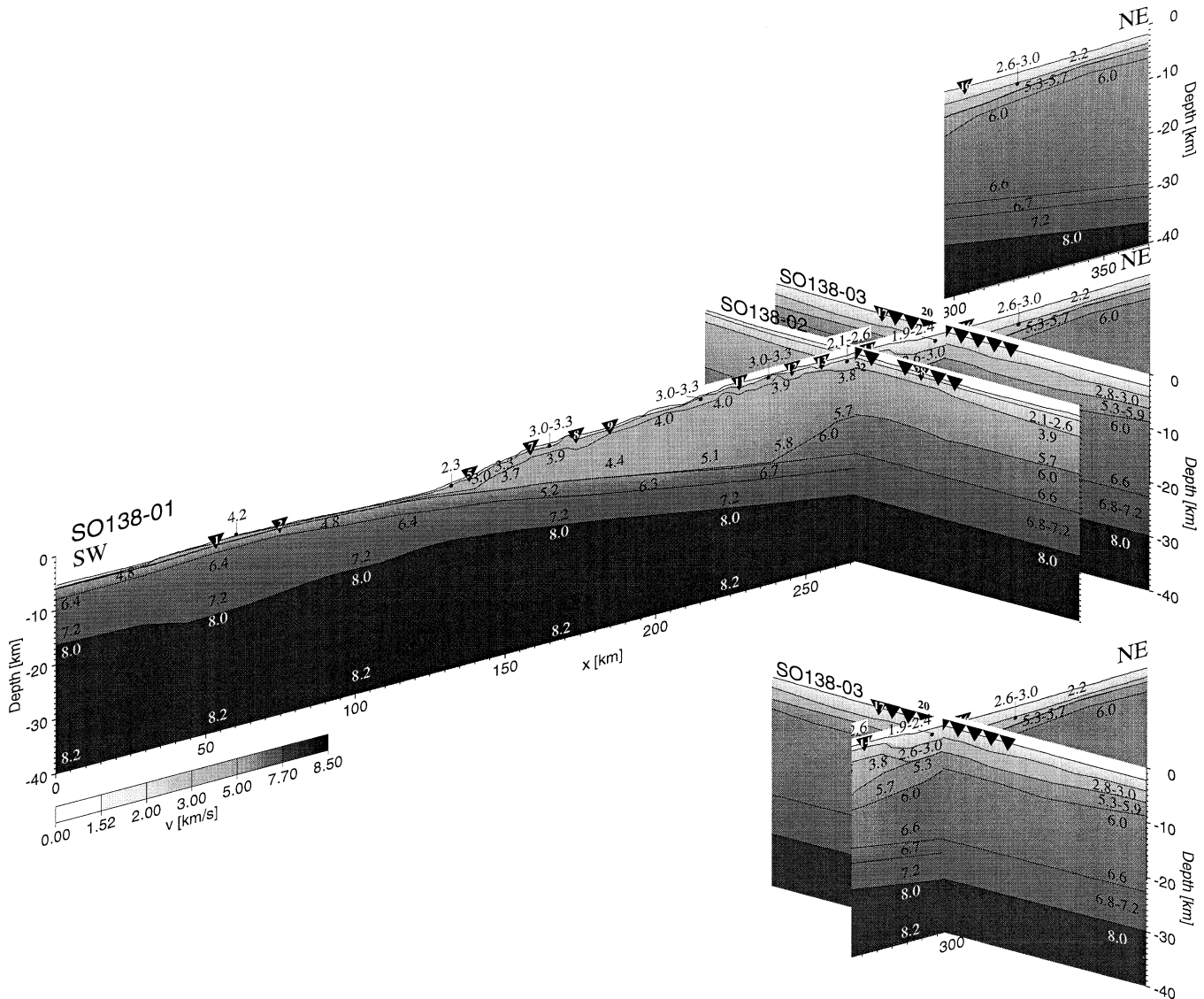


Figure 4. (Continued.)



**Figure 5.** 3-D velocity–depth model across the Sumatra subduction zone. The extra panels show the hidden sections of the dip-line. The dip of the subducted plate is verified to a depth of more than 30 km as it is recorded along the dip-line SO138-01 and along strike-lines 02 and 03. The massive outer high separates the active accretionary domain from the forearc basin and displays moderate velocities reaching  $5.8 \text{ km s}^{-1}$  at almost 20 km depth. The velocity structure beneath the forearc basin is indicative of continental crust.

the top of the plate is imaged at about 7 s, but interferes with the strong sedimentary phases at offsets of less than 20 km. A weaker Moho reflection is recorded at 22 km depth beyond the critical angle  $i_{\text{crit}}$  at about 30 km offset to the northeast. From the trench to beneath the crest of the outer high, clear  $P_{\text{loc}}$  and corresponding  $P_{\text{oc}}$  phases as well as a strong  $P_m P$  are recorded by station OBH 08 (Fig. 9). Beyond the critical angle  $i_{\text{crit}}$ , the crust–mantle boundary causes high amplitudes at up to 50 km offset beneath the outer high. The clearest  $P_m P$  reflections are observed on the record sections of stations 12 and 13. OBH 12 (Fig. 10) constrains the plate dip beneath the outer high, where a strong wide-angle  $P_m P$  is observed at 35–50 km offset to the southwest along profile km 195–208. Station 13 (Fig. 10) recorded the Moho to a depth of approximately 25 km. Beneath the forearc basin, the top of the oceanic plate and the crust–mantle boundary unfortunately interfere with the strong multiple of the basement (e.g. positive offsets on OBH 13 in Fig. 10), so they cannot be clearly identified here.

The velocity structure of the active accretionary prism and the outer high was mainly determined from stations 05–13. Phases  $P_{\text{sed1}}$  and  $P_{\text{sed2}}$  (Figs 8–10) are refracted through the upper sedimentary layers of the accretionary prism and outer high above the basement top, which was identified from MCS data. The lower part of the accretionary complex is covered by refracted phases  $P_{\text{lac}}$ . The backstop structure that marks the transition from the active accretionary prism to the outer high is observed in the MCS data (Fig. 3a) and coincides with a slope break at the seafloor. It appears as a pronounced, landward-dipping reflection that runs from the seafloor slope break down to near the top of the subducted plate. This transition from the active accretionary domain to the outer high is also evident in the velocity structure. At the frontal part of the accretionary complex between the deformation front and the backstop structure, velocities increase laterally from  $c. 3.0 \text{ km s}^{-1}$  to over  $4.0 \text{ km s}^{-1}$  (Fig. 5). Beyond the backstop structure in the outer high, velocities remain constant from



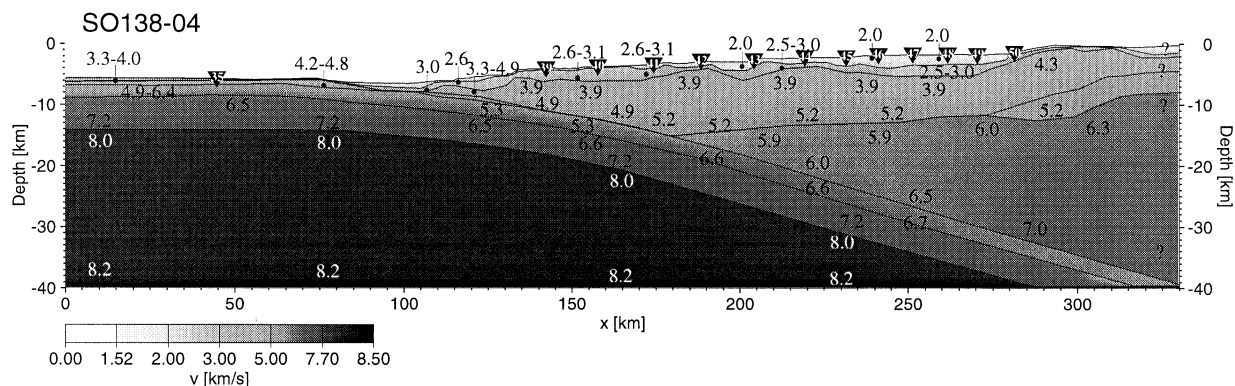


**Figure 6.** 2-D velocity–depth model along refraction line SO138-04 of the Sunda Strait transect. The subduction complex and the forearc domain show a laterally homogeneous velocity structure manifested in an approximately 9 km thick layer comprising the lower accretionary complex. Laterally increasing velocities are found within the active accretionary prism. The Java shelf around profile km 300 is located within Sunda Strait, where a shallow basement with velocities exceeding  $4.3 \text{ km s}^{-1}$  is found.

the slope break to the crest of the outer high. Here, velocities increase slowly with depth and reach values of  $5.8 \text{ km s}^{-1}$  at 18 km depth. This smooth velocity field of the outer high is manifested in phases  $P_{\text{lac}}$  recorded by the stations on the outer high (e.g. OBH 08 in Fig. 9 and OBHs 12 and 13 in Fig. 10). The seafloor topography of the active accretionary prism is characterized by two pronounced accretionary ridges around CDPs 27 300 and 27 000. In addition, small recent ridges are recognized immediately landwards of the deformation front at profile km 40 (Fig. 3a). The rugged seafloor topography of the active accretionary wedge prevails along the seaward part of the outer high until the crest at CDP 21 000. The accretionary prism is disturbed by a number of imbricate thrust faults (Fig. 3a) that appear as landward-dipping reflections cutting down from the seafloor deep through the wedge. A high degree

of deformation expressed in large faults (e.g. near CDPs 23 700 and 25 100) is also characteristic of the seaward part of the outer high (Figs 3a and b). Landwards of the crest, pelagic sediment cover becomes visible and ponded sediment is trapped in several basins formed by the rugged basement top (Fig. 3b). The seaward part of the forearc basin is characterized by two anticlinal folds (Fig. 3c) that mark the position of the Mentawai fault zone between CDPs 15 700 and 16 900. Folding there is still active and involves the entire sedimentary column and crops out at the seafloor as a large, 15 km wide bulge. The Mentawai fault zone divides a smaller sub-basin from the main forearc basin. A maximum of 5 km sediment infill is recorded in the main basin, compared to approximately 3 km seaward of the Mentawai anticline in the sub-basin. The variation in seafloor depth between the two basins equals

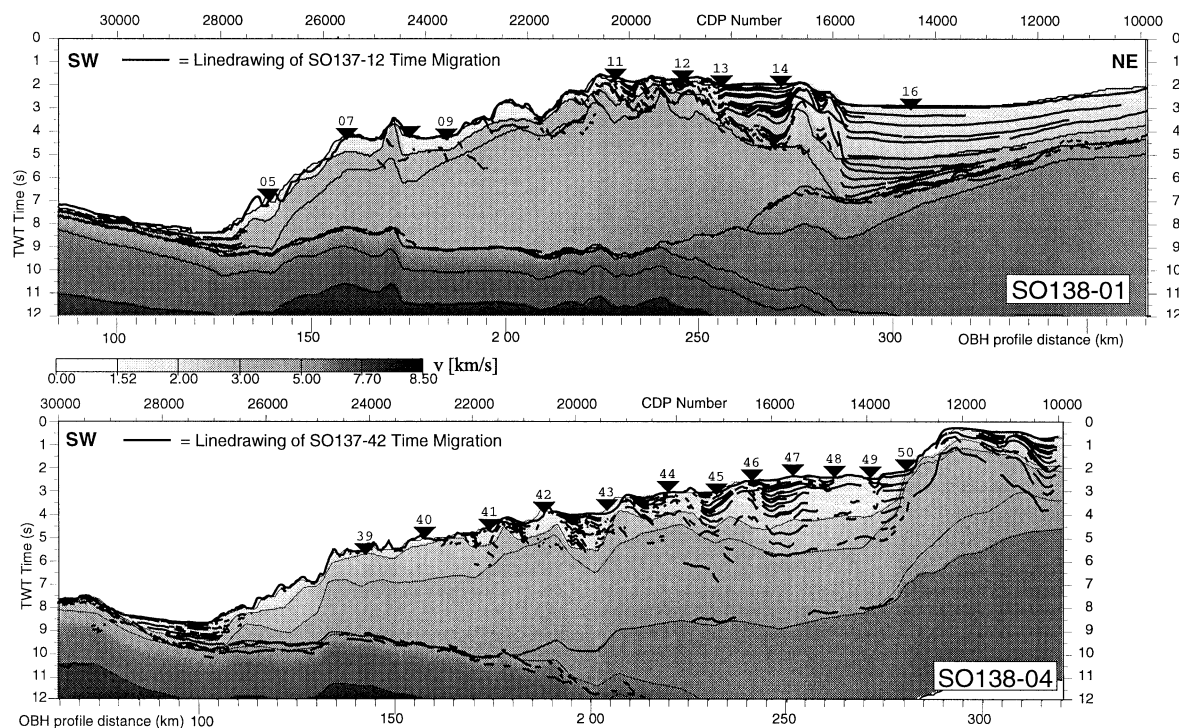


**Figure 7.** Time-converted sections of the velocity–depth models from the two dip-lines are overlain by line drawings of the corresponding reflection lines show a good correlation between the main units. The modelling of the upper parts of the velocity–depth sections is based on the results from the MCS data.

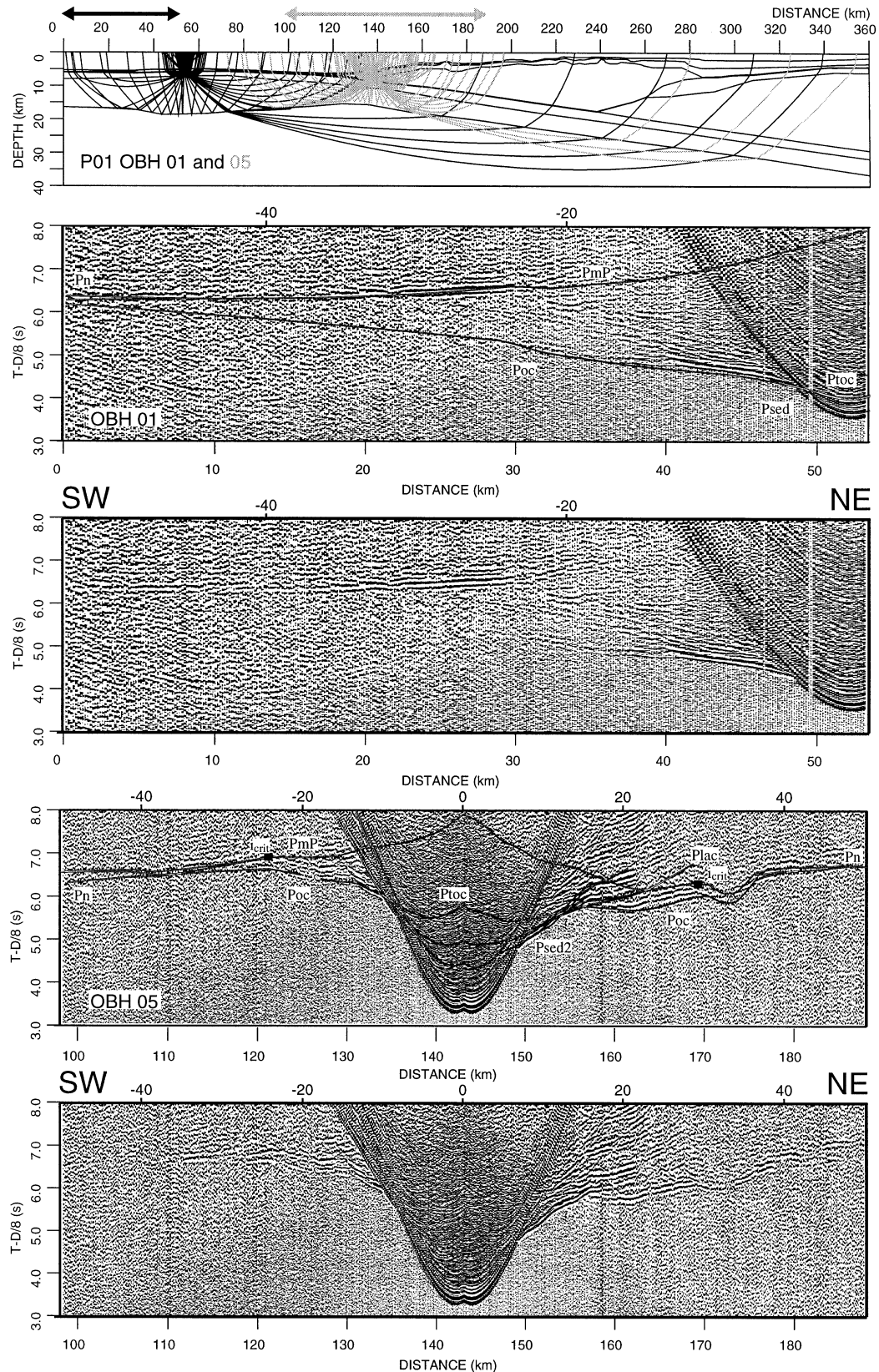


**Figure 8.** Record sections from two stations (OBHs 01 and 05) deployed along the dip-line SO138-01. The uppermost image displays the ray paths through the model subsurface for both stations. Thick arrows indicate the offsets displayed in the record sections of the corresponding stations. The data are shown with modelled traveltimes overlain in the upper images, whereas the raw data set is displayed in the lower sections. Refer to Table 1 for phase nomenclature. OBH 01 is located on the incoming plate and records a local thickening of the igneous oceanic crust. Mantle phases ( $P_mP$  and  $P_n$ ) record normal upper mantle velocities of  $8.0 \text{ km s}^{-1}$ . Station 05 is the first station landwards of the deformation front documenting the downthrusting of the oceanic plate, which shows a normal thickness of 7.5 km. The offset of the critical angle is marked by a black square.

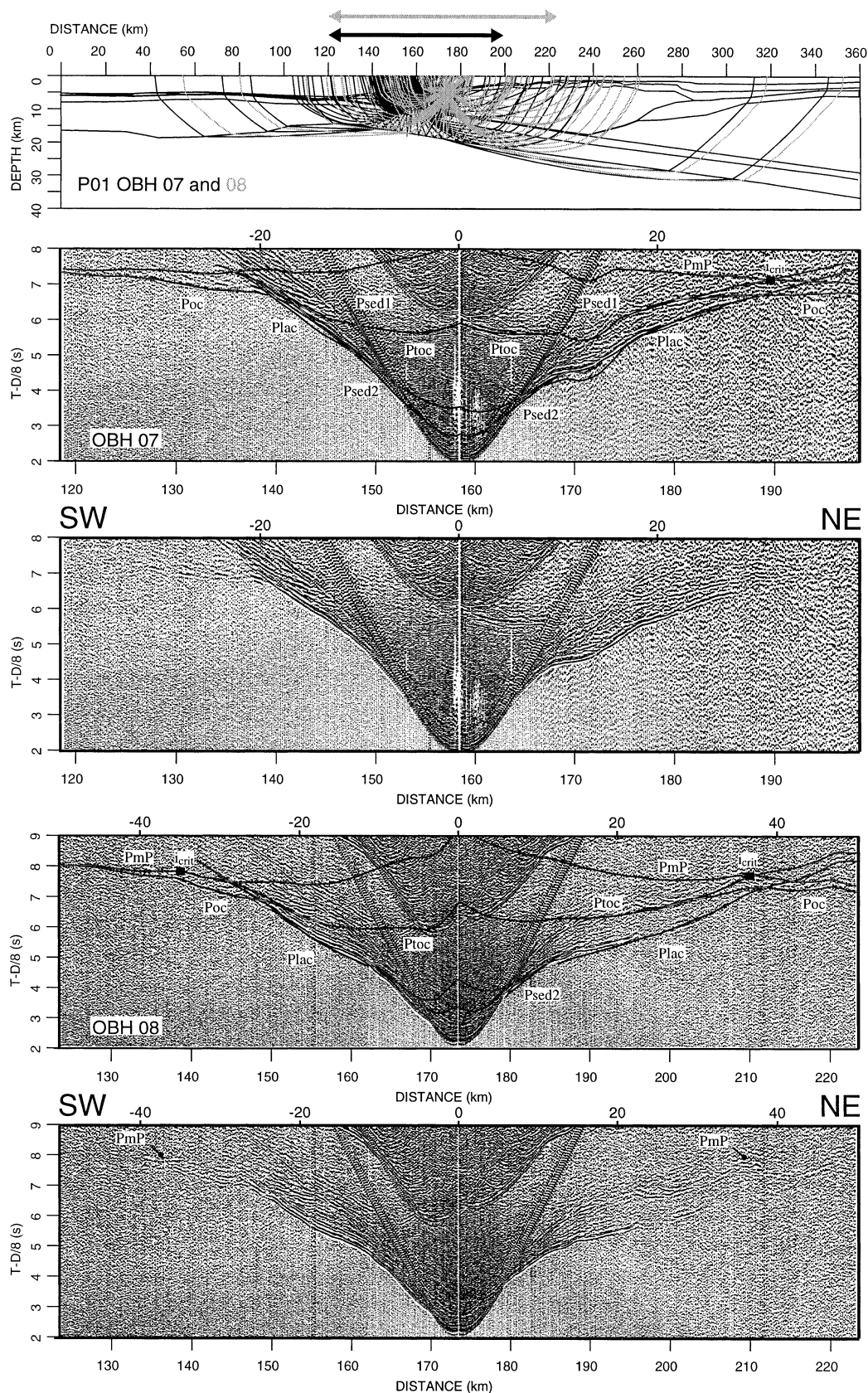


**Figure 9.** Record sections and ray diagram for two stations (OBHs 07 and 08) deployed along line SO138-01. For further information, refer to Fig. 8. OBH 07 of profile SO138-01 is deployed on the outer high. The velocity structure of the outer high is documented by the sedimentary phases  $P_{\text{sed1}}$  and  $P_{\text{sed2}}$  for the upper parts and by phase  $P_{\text{lac}}$  for the lower accretionary complex. A strong near-vertical-incidence reflection  $P_{\text{toc}}$  from the subducted slab is present at positive offsets. High amplitudes of the  $P_{\text{mP}}$  reflection are visible beyond the critical angle to the northeast. OBH 08 also records the crust–mantle boundary beyond the critical angle.

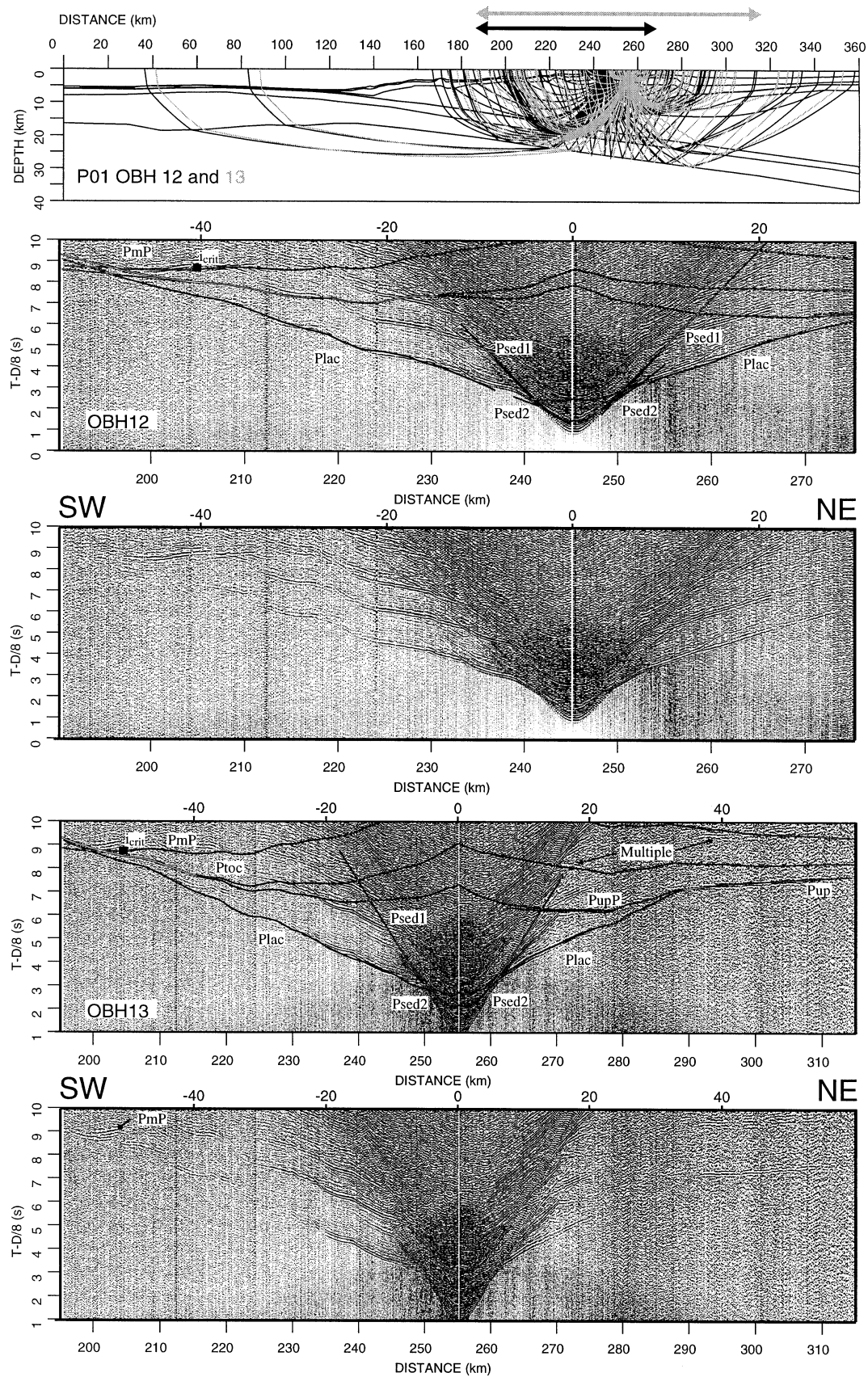


**Figure 10.** Record sections and ray diagram for two stations (OBHs 12 and 13) deployed along line SO138-01. For further information, see Fig. 8. OBHs 12 and 13 are the landwardmost stations located on the outer high. Both instrument recordings reflect the smooth velocity structure of the outer high recorded by the sedimentary phases  $P_{sed1/2}$  and  $P_{lac}$ . The oceanic Moho is recorded by seaward-travelling phases  $P_mP$ . Beneath the forearc basin the leading edge of the upper plate is recorded by phases  $P_{up}P$  and  $P_{up}$  of OBH 13.



almost 600 m. A clear bottom-simulating reflector (BSR) is visible crossing the anticline, but is difficult to trace in the subparallel strata of the forearc basin and sub-basin (Fig. 3c). The sedimentary units in the forearc basin show little deformation as they progressively thin towards the northeastern end of the profile. Seismic velocities increase from about 1.9–2.0 to 3.0 km s<sup>-1</sup> in the sedimentary strata (Fig. 5). The underlying basement top is found at approximately 6 s two-way traveltimes (TWT) where the basin is deepest near the Mentawai fault (Fig. 3c). The basement top, which is marked by a high-amplitude, low-frequency band of energy, continues beneath the anticlinal feature and is still traceable beneath the sub-basin seawards of the Mentawai fault zone. Towards the Sumatra shelf the seismic signature of the basement top changes significantly at profile distance 240 km (Fig. 3c). A 2 km thick layer with velocities increasing from 5.3 to 5.7 km s<sup>-1</sup> marks the basement top (Fig. 5), beneath which higher velocities, ranging from 6.0 to about 6.6 km s<sup>-1</sup> at greater depth, dominate. This lower unit is evident in phases  $P_{up}P$  (OBH 13 in Fig. 10) and the corresponding refracted wave  $P_{up}$  and extends beneath the outer high, where it forms the leading edge of the overriding plate.

#### 4.2 Strike-lines SO138-02 and SO138-03

The seismic grid was extended by two strike-lines to gain additional constraints on the configuration of the subducted plate. Profile SO138-02 lies along the strike of the aforementioned sub-basin, about 140 km landwards of the deformation front (Fig. 2). The line shows some topographic variation, amounting to about 1 km seafloor elevation difference along the profile. The velocity–depth model that was derived with the incorporation of mini-streamer reflection data recordings (not shown here) (Flueh 1999), shows a substantial variation in sediment thickness of the upper sequences, which increases from about 2 km to almost 4 km at the southeastern end of the profile. It is evident from the mini-streamer recordings that strong deformation of the sedimentary strata occurs as folding and partial stacking of the sequences. Compressional tectonic activity is ongoing and the entire upper sedimentary units as well as the seafloor are affected. Phases  $P_{sed1}$  and  $P_{sed2}$  travelling through these units (Fig. 11) represent velocities ranging from less than 2.0 km s<sup>-1</sup> at the top to 2.6 km s<sup>-1</sup> in the lower parts (Fig. 5). The underlying 7–9 km thick unit of the lower outer high (represented by refracted waves  $P_{lac}$ ) is bounded at the base by a velocity step from 5.7 to 6.0 km s<sup>-1</sup> (Fig. 5). This boundary has been recorded as a clear  $P_{up}P$  reflection at about 11 km depth (e.g. OBHs 28 and 32 in Fig. 11). Whereas the top of the subducted plate could not be identified unambiguously beneath this layer by stations deployed along the dip-line SO138-01, it is present as a strong arrival on several record sections along both strike-lines. Stations 28 and 32, which are presented here, record the top of the subducted oceanic crust at 19 km depth as reflection  $P_{toc}$  (Fig. 11).

Along strike-line SO138-03, which is located 170 km landwards of the deformation front, the sedimentary infill of the forearc basin reaches a thickness of 4 km ( $P_{sed1}$  and  $P_{sed2}$  in Fig. 12). Water depth varies little along the profile and subparallel stratification of the sedimentary units yields a very smooth velocity–depth model (Fig. 5). Phases  $P_{up}$  through the upper plate basement reveal velocities of 6.0 to 6.6 km s<sup>-1</sup>

there. The downgoing plate is only identified from a wide-angle reflection at the southeastern end of the profile, beyond the critical angle  $i_{crit}$ . High amplitudes of phase  $P_{toc}$  (OBHs 17 and 20 in Fig. 12) locate the top of the downgoing slab at 22–23 km depth there. The profile is too short to record the oceanic Moho. The depth of the subducted plate found along the strike-lines is in perfect agreement with the results from the dip-line, as seen in Fig. 5.

#### 4.3 Sunda Strait transect

The second transect runs across the subduction complex further to the southeast, covering parts of the ocean basin and the accretionary complex and ending on the Java shelf within the Sunda Strait (Fig. 2). Only the part of SO137-42 that is coincident with the wide-angle profile P04 is shown in Fig. 4. OBH profile SO138-04 is 330 km long. 13 instruments, from which selected data are shown in Figs 13–15, successfully recorded data. Unfortunately, instrument failure occurred in the vicinity of the trench. Thus the structure of the incoming oceanic plate is deduced only from sections of OBH 35 (Fig. 13), which show a 7.5 km thick crust with a typical oceanic velocity–depth distribution. A  $P_mP$  reflection records the Moho at 14 km depth. Immediately seawards of the trench (km 15–35 in Fig. 4a) a local seafloor elevation not covered by sediment shows some normal faulting. The trench is 20 km wide, carrying an infill with a maximum thickness at the deformation front of 1.5 km, as inferred from the MCS data (Fig. 4a).

A clear image of the active accretionary domain is presented in Fig. 4(a), in which at least five accretionary ridges are recognized, composing an accretionary wedge above the downgoing plate and bounded to the northeast by a sharp backstop structure at the slope break. Imbricate thrust faulting in this frontal part documents the deformation of the accreted sediments as they are pushed against the active backstop. Seismic velocities increase laterally from 3.0 km s<sup>-1</sup> at the deformation front to about 3.9 km s<sup>-1</sup> near the backstop structure (Fig. 6), supporting the notion of active accretion here. The upper sedimentary layers have been modelled with the help of the MCS data (Fig. 7). Seismic velocities derived from the upper sedimentary units range from 2.0 km s<sup>-1</sup> to approximately 3.0 km s<sup>-1</sup> (Fig. 6). Towards the Java shelf, approximately between CDPs 13 000 and 18 000, the sedimentary phases  $P_{sed1}$  and  $P_{sed2}$  are more distinct (e.g. in the record section of OBH 46; Fig. 15), as the seafloor topography is smoothed by the thicker sediments accumulated here. A bright BSR is identified mimicking the seafloor between CDPs 14 000 and 17 000 approximately 400–500 ms TWT below the seafloor (Fig. 4c). No sediment cover is found on the Java shelf onset, where a change in seafloor depth of more than 1200 m occurs over a distance of 10 km. Thicker sedimentary sequences are again present at the northeastern end of the profile in a small basin on top of the Java shelf within Sunda Strait (CDPs 10 000–12 000 in Fig. 4c), whereas little sediment can be recognized further seawards up to CDP 13 000.

For the greater part of the profile, between the active backstop and the Java shelf onset, little lateral velocity variation is recognized beneath the sedimentary units. Numerous faults are visible beneath the outer high, some of which extend to near the top of the subducted plate (Fig. 4b). The basement top marks a velocity step from approximately 3.0 km s<sup>-1</sup> at the base of the sedimentary layers to 3.9 km s<sup>-1</sup> (Fig. 6). A roughly 9 km



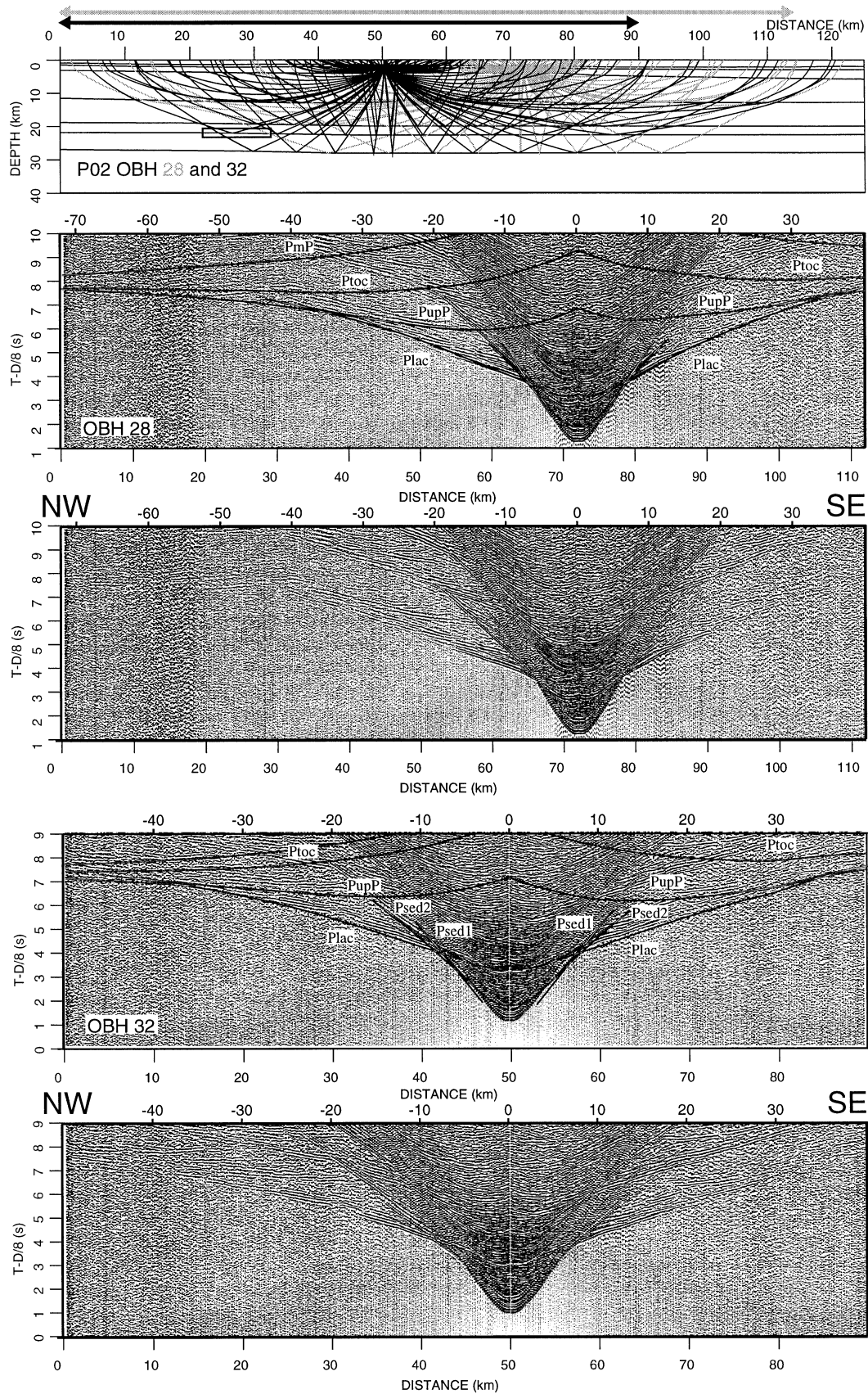


**Figure 11.** Record sections and ray diagram for stations 28 and 32 along strike-line SO138-02. For further information, see Fig. 8. Both stations record the leading edge of the upper plate beneath the outer high ( $P_{up}P$ ) as well as the top of the subducted plate ( $P_{toc}$ ). The distinct phase recognized on the section of OBH 32  $\approx 0.7$  s after reflection  $P_{toc}$  is caused by a discontinuous intracrustal reflector, as indicated by the black box in the ray path diagram. This phase is not observed at any other station.

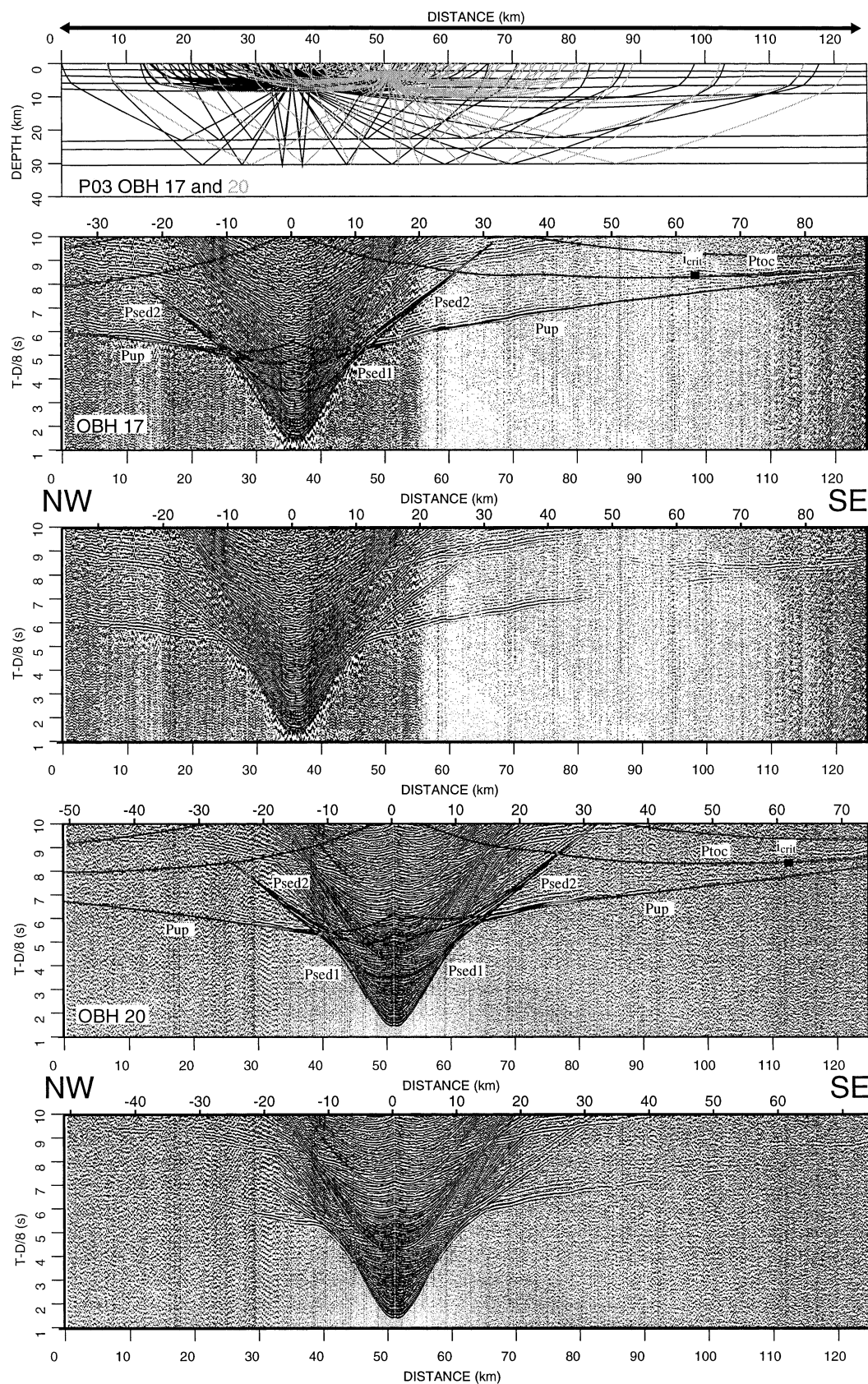


**Figure 12.** Record sections and ray diagram for two stations (OBHs 17 and 20) deployed along strike-line SO138-03. For further information, see Fig. 8. Stations OBHs 17 and 20 cover the seaward part of the forearc basin off southern Sumatra. The thick sedimentary strata are recorded by phases  $P_{sed1}$  and  $P_{sed2}$ . The basement beneath the forearc basin is represented by phase  $P_{up}$ . The top of the subducted plate was recorded by both stations beyond the critical angle of phase  $P_{toc}$ . While the downgoing slab was not recorded beneath the forearc basin along the dip-line, it is present on the record sections of several stations deployed along strike-line 03.

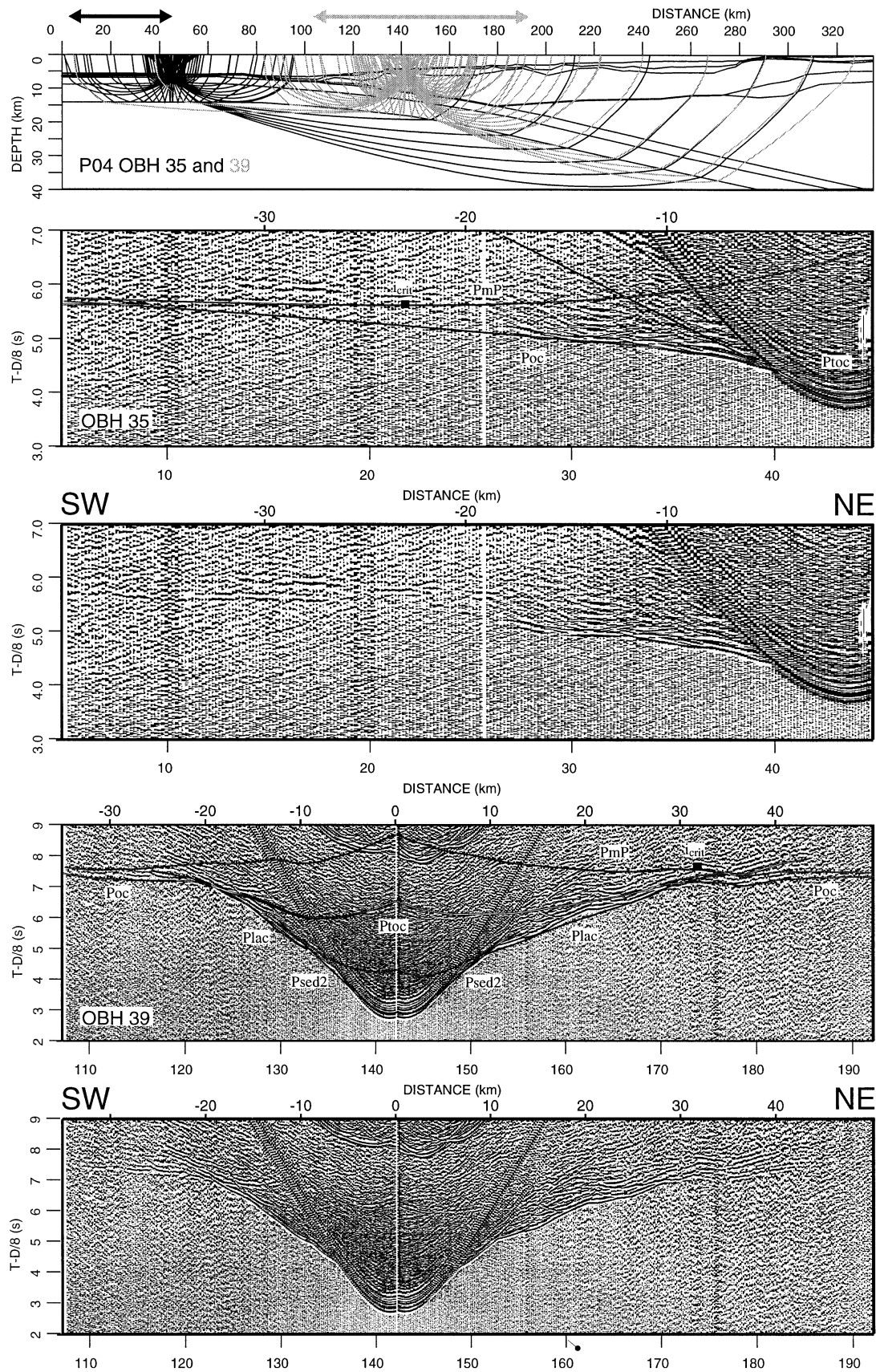


**Figure 13.** Record sections and corresponding ray paths of stations OBHs 35 and 39 deployed along the Sunda Strait transect SOI38-04. For further information, see Fig. 8. OBH 35 is the only instrument recording data seawards of the trench. A 7.5 km thick oceanic crust showing a normal seismic velocity structure is found here. OBH 39 is the first instrument located landwards of the deformation front on the active accretionary domain. The geometry of the subducted plate is constrained by phases  $P_{\text{loc}}$ ,  $P_{\text{oc}}$  and  $P_{\text{mP}}$ .



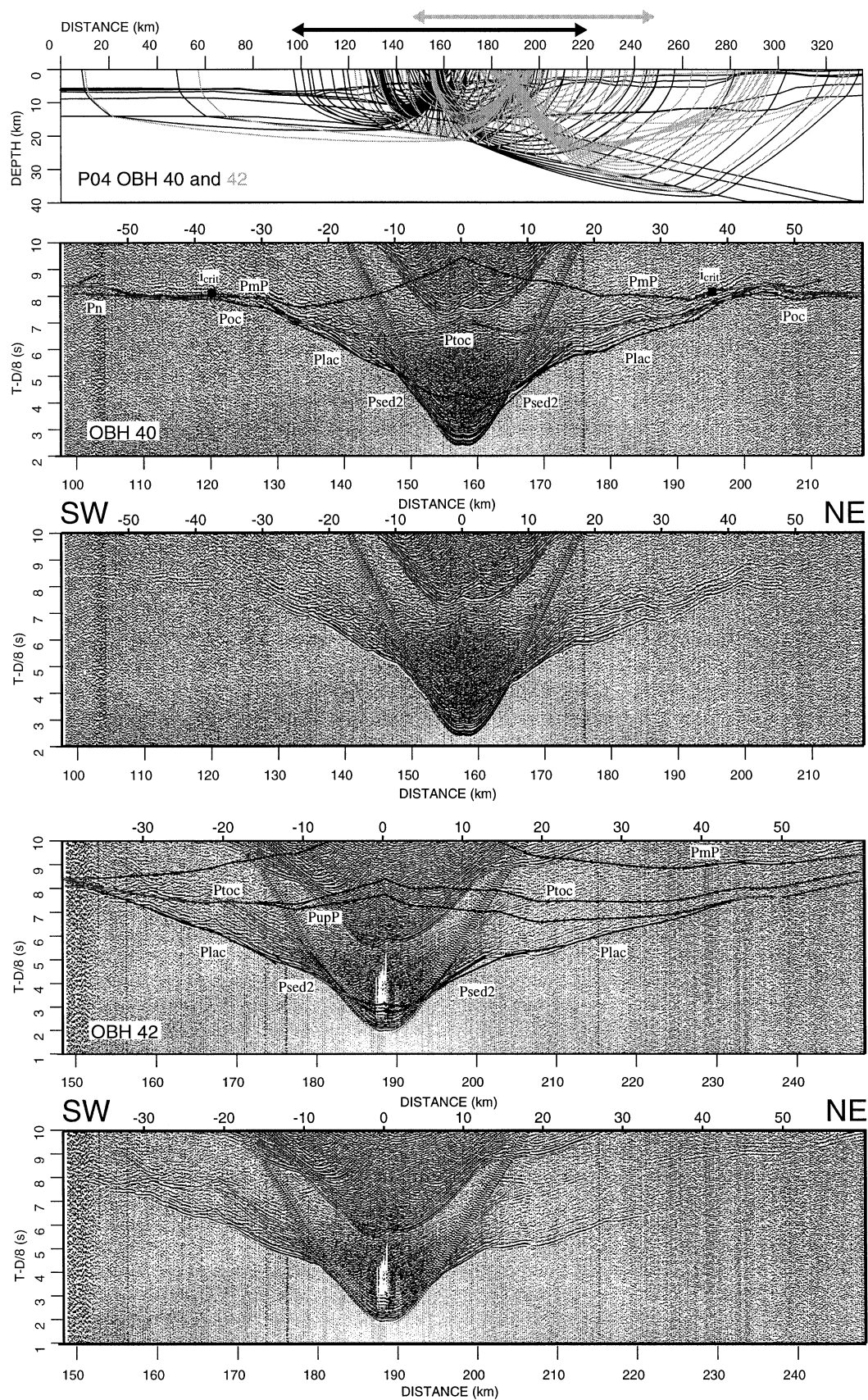


**Figure 14.** Record sections and corresponding ray paths of stations OBHs 40 and 42 deployed along line SO138-04. For further information, see Fig. 8. OBHs 40 and 42 were deployed along the outer high. Station 40 recorded an oceanic  $P_n$  phase at negative offsets as well as the corresponding  $P_mP$ . The top of the subducted plate is recognized in phases  $P_{toc}$  and  $P_{ocr}$ . The smooth velocity structure of the outer high domain is documented by phase  $P_{lac}$ . OBH 42 recorded a strong  $P_mP$  at positive offsets, tracing the oceanic Moho to a depth of more than 30 km.

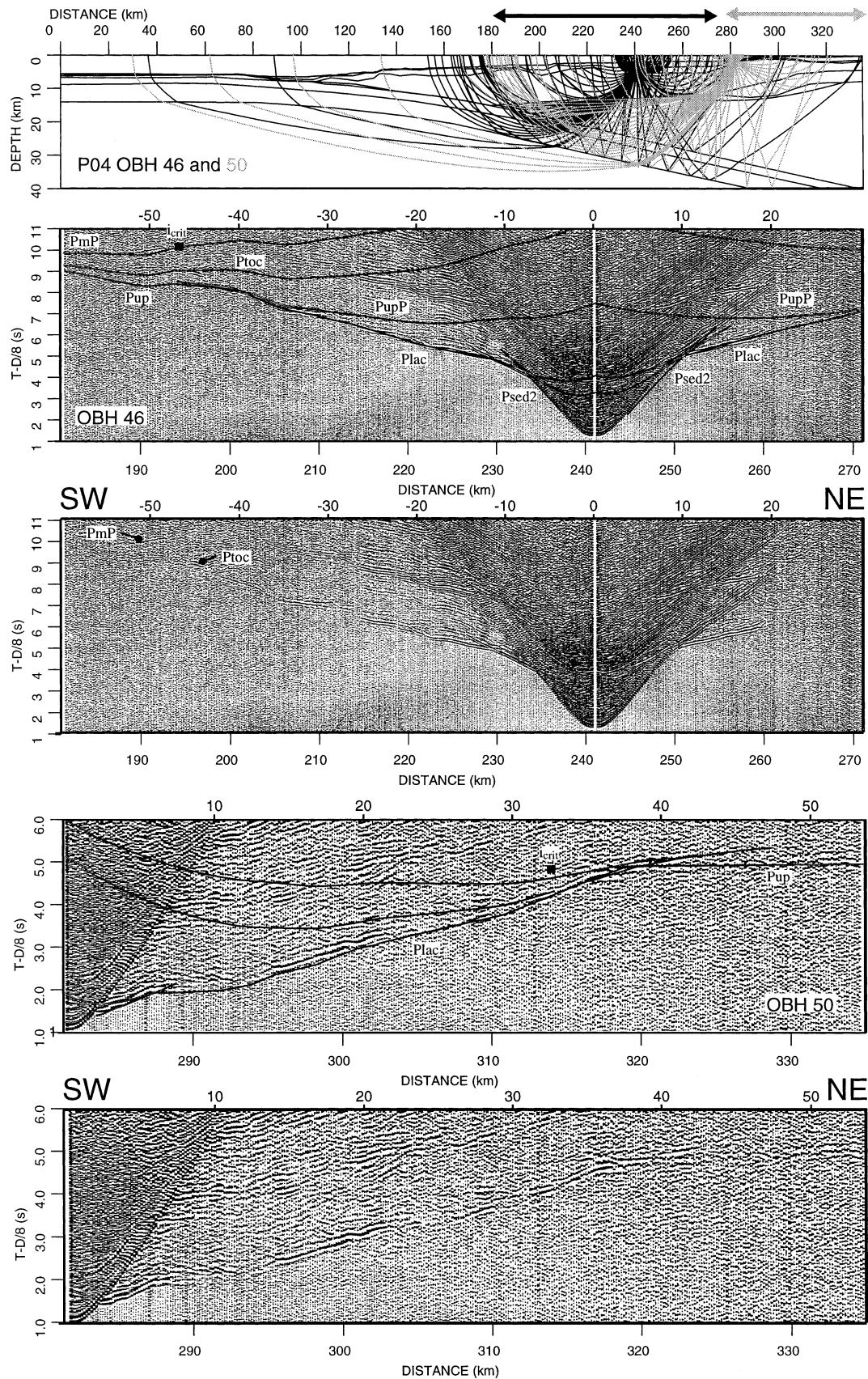


**Figure 15.** Record sections and corresponding ray paths of stations OBHs 46 and 50 deployed along profile SO138-04. For further information, see Fig. 8. Both stations presented here are located within the forearc domain off Sunda Strait. OBH 46 recorded the leading edge of the upper plate in the arrivals of  $P_{up}P$  and  $P_{up}$  as well as the oceanic Moho at offsets beyond  $-50$  km. Station 50 is deployed close to the Java shelf onset and covers the basement ridge at positive offsets. Refraction  $P_{up}$  verifies the elevated velocity values found here (see Fig. 6).



thick uniform layer, which shows some thinning below the larger sedimentary basins immediately seawards of the Java shelf onset, represents the lower accretionary complex. The smooth velocity field is documented by phases  $P_{\text{lac}}$  recorded by the various stations positioned along the outer high and forearc domain (OBHs 40, 42, 46 in Figs 14 and 15). A uniform velocity increase with depth from 3.9 to 5.2 km s<sup>-1</sup> is recognized for the main part of the lower outer high-forearc domain (Fig. 6). The frontal, most seaward part of this layer thins progressively towards the deformation front as it is bounded at the base by the subducted slab. Velocities at the base range from 3.9 to 4.9 km s<sup>-1</sup>. This is evident from seaward-travelling phases  $P_{\text{lac}}$  recorded by stations OBHs 39 and 40 (Figs 13 and 14). The base of this layer is found at a depth of approximately 13 km, except for the aforementioned thinned portion (profile km 250–280 in Fig. 6), where the layer boundary is found at 12 km depth. In the seaward portion of the deepest crustal layer of the upper plate, velocities increase to 5.9–6.0 km s<sup>-1</sup>, as is deduced from refracted waves  $P_{\text{up}}$  and their corresponding reflections  $P_{\text{up}}P$  of station OBH 46 in Fig. 15. As OBH 46 also records the top of the subducted plate ( $P_{\text{toc}}$  in Fig. 15) beneath the leading edge of the upper plate, the low velocity–depth gradient is verified there.

A different situation emerges below the Java shelf. A substantial velocity increase is observed and velocity values of 4.3 km s<sup>-1</sup> are recorded immediately below the seafloor as the recent sedimentary cover there is negligible. The northeastward phases recorded by OBH 50 (Fig. 15) travel through the Java shelf ( $P_{\text{lac}}$ ). Refracted  $P_{\text{up}}$  arrivals show a lateral velocity increase also within the lower portion of the upper plate, where values of 6.3 km s<sup>-1</sup> are detected at 12 km depth.

The downthrusting plate is present in the MCS data as a high-amplitude band of energy showing a high degree of coherence, especially beneath the frontal accretionary prism (Figs 4a and b). This event can be followed for about 110 km from the deformation front, although the landward portion is partially inhibited by remnants of the seafloor multiple. Numerous large, landward-dipping faults are recognized in the oceanic crust (e.g. beneath CDPs 27 000–27 600). Several OBH stations track the subducted plate. OBH 39 (Fig. 13) records a clear near-vertical-incidence reflection  $P_{\text{toc}}$ , as well as the corresponding wide-angle reflection and the refracted wave  $P_{\text{oc}}$ . The crust–mantle boundary is imaged by a  $P_{\text{m}}P$  at offsets from 20 km to over 40 km distance down to a depth of more than 20 km. The next instrument (OBH 40 in Fig. 14) recorded a seaward-travelling  $P_{\text{n}}$  phase. Station 42 traces the Moho down to 35 km depth beneath the forearc domain (Fig. 14) while tracking the top of the plate at southwestern offsets down to 15 km. The deepest response from the downgoing plate was recorded by OBH 46 (Fig. 15), which shows increased amplitudes beyond the critical angle,  $i_{\text{crit}}$ , of the  $P_{\text{m}}P$  reflection at more than 30 km depth and a reflection  $P_{\text{toc}}$  from the top of the plate. These events allow us to trace the downthrusting plate to a depth of more than 30 km.

#### 4.4. Gravity modelling

In addition to seismic data modelling, we also used the gravity field to test the plausibility of our velocity–depth models. Gravity calculations were conducted for both dip-lines, SO138-01 and SO138-04. The gravity model incorporates the structures found in the wide-angle forward modelling, to which density values as

displayed in Figs 16(b) and (d) were assigned. Using *a priori* information about the main geological units is crucial to limiting the number of possible solutions that fit the gravity data. We based our selection of the density values on the relationship between compressional velocities and densities. Average densities of 2.23 and 2.4 g cm<sup>-3</sup> (Ludwig *et al.* 1970) were assigned to the upper sedimentary layers, which show velocities <3.0 and <4.0 km s<sup>-1</sup>, respectively. For the lower accretionary complex, densities ranging from 2.5 to 2.7 g cm<sup>-3</sup> correspond to the higher degree of compaction and the greater overburden there. A uniform density value of 2.89 g cm<sup>-3</sup> as suggested by Carlson & Raskin (1984) was assumed for the entire oceanic crust (Figs 16b and d). Lower crustal densities of 2.95 g cm<sup>-3</sup> beneath the forearc domain of the upper plate correspond to values derived from the relationship of Barton (1986). Density values of 3.37 g cm<sup>-3</sup> are associated with the c. 90 Myr old lithosphere. The calculated gravity response (black dotted line in Figs 16a and c) was then compared to ship data acquired during the cruise (grey line in Figs 16a and c) (Heyde *et al.* 2000).

Along line SO138-01 gravity variations of up to 170 mgal occur (Fig. 16a). The most pronounced features are the two distinct gravity lows caused by the deep trench and the forearc basin, respectively. The gravity high, reaching values of up to 40 mgal seawards of the trench, is associated with a shallower seafloor. The rugged topography of the basement top beneath the outer high is expressed in pronounced gravity variations between the trench and the forearc basin (between km 200 and 280 in Fig. 16b). The gravity response of the landward part of the forearc basin is already influenced by the higher densities of the upper plate modelled with uniform values of 2.95 g cm<sup>-3</sup> (Fig. 16b). Our calculations fit the observed gravity field to within  $\pm 10$  mgal (Fig. 16a) and thus, to a first-order approximation, the 2-D modelling corresponds adequately to the ship survey data. A detailed fit was achieved for the ocean basin and the active accretionary domain, as well as for the forearc basin. Without further efforts to gain a better fit along the outer high, the calculated values match the observed data sufficiently. The main trend of the gravity field across the subduction complex could be matched, which yields further information on the geometry of the downgoing slab.

Gravity variations of up to 250 mgal are present along the Sunda Strait transect, mainly caused by the high positive values associated with the Java shelf (Fig. 16c). Like the other line, the trench and forearc domains cause distinct gravity lows around profile km 110 and 240 (grey line in Fig. 16c), as is expected from the great depth of the trench and the thick sedimentary sequences observed in the forearc domain. Again, without further efforts to achieve an overall superior fit, a detailed match was nonetheless achieved for the main part of the profile (black line in Fig. 16c), except for the seawardmost 40 km and the Java shelf onset. As the basement top is not as intensely expressed in the MCS data as in the Sumatra transect, gravity values across the outer high are distinctly smoother on the Sunda Strait profile. The lower accretionary complex was modelled with density values ranging from 2.5 to 2.6 g cm<sup>-3</sup>, except for the more unconsolidated sediments at the frontal part near the deformation front (Fig. 16d). The high gravity values found in the Java shelf correspond to the increased velocities there. Gravity values decline towards the north-eastern end of the line at profile distances greater than 290 km (Fig. 16d), where a sedimentary basin is observed in the MCS

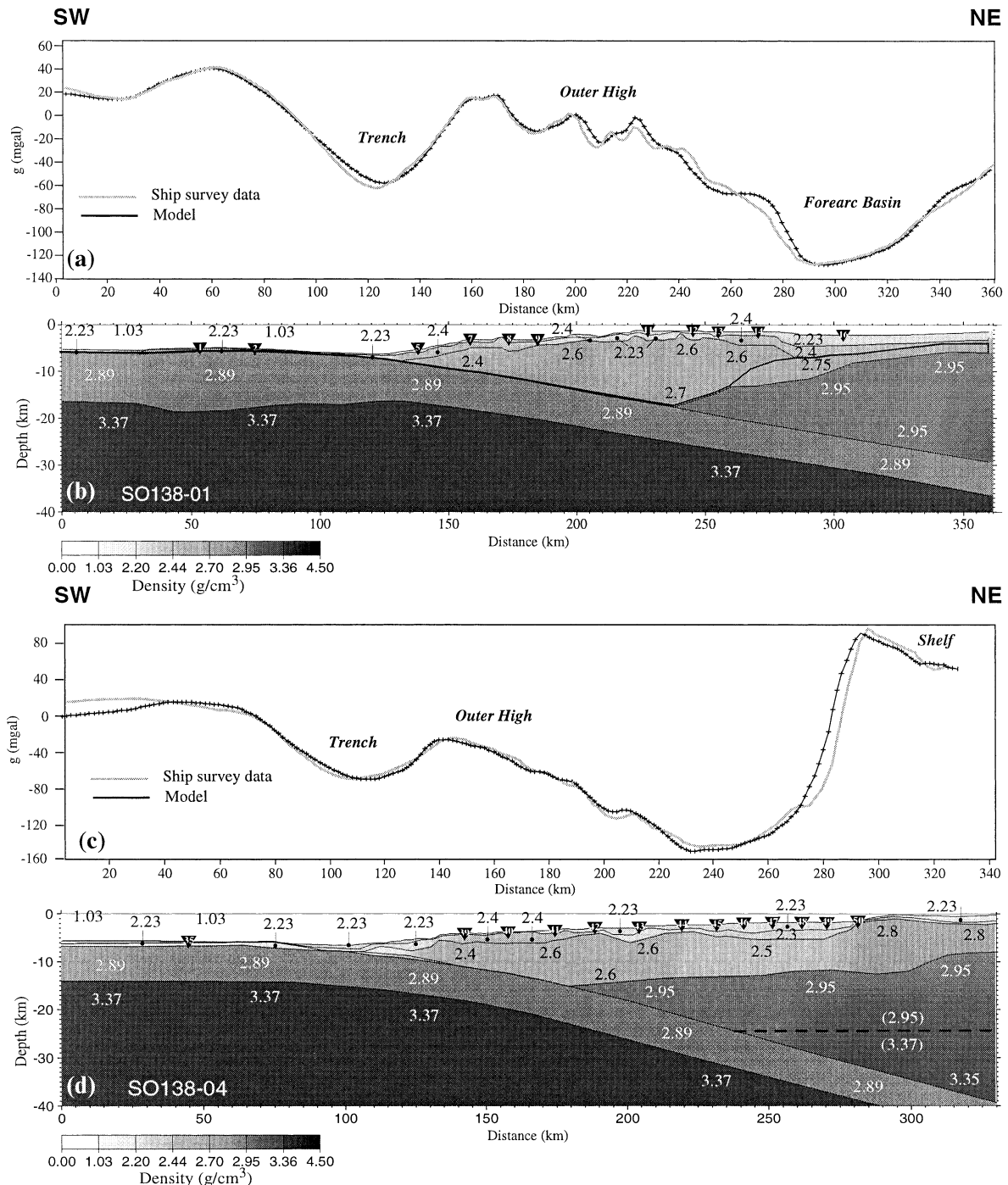


**Figure 16.** Gravity modelling for dip-lines SO138-01 and SO138-04. The ship survey data (black lines in a and c) are compared to the gravity response (grey lines in a and c) derived from the density models shown in (b) and (d). Density values were assigned to the velocity structures derived from forward modelling of the OBH data. The ship gravity survey during the GINCO project was conducted by the BGR in Hannover, Germany (Heyde *et al.* 2000). The gravity calculations presented here confirm the plate geometry across the subduction complex. Along line SO138-04 the approximated upper plate Moho is indicated by a dashed line.

data (Fig. 4c). Although no upper plate Moho phases could be identified in the seismic data beneath the forearc domain, the gravity response allows an estimate of Moho depth, as shown in Fig. 16(d). When the upper plate layer with a density gradient ranging from 2.95–3.35 g cm<sup>-3</sup> is substituted by two layers modelling the crust–mantle transition with a density

increase from 2.95 to 3.37 g cm<sup>-3</sup>, the gravity fit remains unchanged. As no corresponding boundary is present in the seismic data, this approximation is solely based on the gravity response. However, the overall fit provides an additional constraint on the dip of the subducted plate on this transect, where no wide-angle strike-lines are available.

## 5 DISCUSSION

### 5.1 Igneous oceanic crust and subducted slab

The Sumatra line shows a thickening of the incoming igneous crust seawards of the trench (Fig. 16b). As no similar anomalies have been reported for other parts along the Sunda margin, we interpret this as a local phenomenon. This interpretation is supported by the recordings landwards of the deformation front, which show a subducting slab of normal oceanic crustal thickness (7.5 km) (e.g. as recorded by OBH 05 in Fig. 8). Global satellite gravity (Sandwell & Smith 1997) is too coarse to resolve this crustal anomaly. The Sunda Strait transect displays a 7.5 km thick crust seawards of the trench (Fig. 16d). The velocity–depth functions for both domains show a normal velocity–depth structure with values that have also been reported for Pacific oceanic crustal samples older than 29 Myr (White *et al.* 1992). The closest drilling information from the oceanic basin is available from DSDP Hole 211. It is located at 9.78°S, 102.7°E close to the southwestern end of profile SO137-42. Quaternary and Pliocene pelagic sediments were drilled here before reaching the basement.

Upper mantle velocities of 8.0 km s<sup>-1</sup> are determined from the  $P_n$  phases recorded beneath the oceanic basin by several stations along line SO138-01. As no  $P_n$  was recorded along the Sunda Strait transect, the mantle velocities are gained from the  $P_mP$  reflection recorded by OBH 35, which shows corresponding values. Seismic investigations off western and central Java (Curry *et al.* 1977) found comparable crustal thickness and velocity values.

The trench fill increases by over 25 per cent from 1.1 km off Sumatra to 1.5 km maximum wedge thickness off the Sunda Strait. Since the Sumatra reflection line ceases about 20 km seawards of the trench, only the current material input of approximately 500 m thickness can be determined. A corresponding value is established for recent trench input along the Sunda Strait transect. The Sunda Strait line continues for about 250 km into the ocean basin (Fig. 2). A highly variable basement depth is observed along this segment. In parts the basement crops out above the seafloor, while in other parts it is covered by more than 900 m of ocean basin deposits (Reichert 1999 and this study). Judging from this highly variable thickness, a large part of the sediment cover probably originated as turbidites. Hemipelagic and pelagic sediment would build a smooth cover, whereas thickness variations and basement outcrops are the results of current-driven sedimentation of turbiditic origin. Judging from satellite gravity (Sandwell & Smith 1997), the overall plate structure of the ocean basin within the study area is stable as the large amounts of terrigenous sediment input from the Bengal fan do not cause deviations in the sediment cover this far south. Thus a sediment thickness variation in the ocean basin off southern Sumatra similar to that off Sunda Strait can be expected, hence a difference of 400 m in trench fill thickness is feasible. This is also supported by additional seismic reflection lines collected by the BGR across the trench from north of Enggano island to western Java (Reichert 1999) and by reflection data collected in 1980 by the Scripps Institution of Oceanography (SIO) off central Java (G. Moore, personal communication, 2000). The trench fill thickness varies for up to 1600 m between these lines without showing a regional trend.

The top of the oceanic crust is traced by various stations on both dip-lines as it starts bending beneath the deformation

front (Figs 8–10 and 13–15). An increase in plate dip along the Sumatra transect from less than 3° near the deformation front to approximately 5° beneath the outer high is observed. The Sunda Strait line shows a corresponding increase in plate dip from a little over 4° to 7°. These trends are supported by the gravity modelling conducted along the dip-lines. As no local earthquake or tomographic studies exist, the slab configuration can only be correlated to global earthquake locations, which are, however, not detailed enough in this area to yield any conclusive information. For the Sumatran domain some 3-D constraint is gained from the two strike-lines, which record the downgoing plate at 19 km depth beneath the outer high and at 21 km depth beneath the forearc basin (Figs 11 and 12). In order to verify the observed reflections from the leading edge of the upper plate ( $P_{up}P$ ) and the top of the subducted slab ( $P_{loc}$ ), synthetic data modelling has been attempted using OBH 32 deployed on profile SO138-02 and OBH 20 from profile 03 (Fig. 17). This dynamic modelling approach is based on the reflectivity method, which uses a laterally homogeneous layered model, for which the reflectivity is calculated analytically from the seismic velocities, densities and attenuation factors of the layers. The resulting synthetic sections are compared to the real data. The refraction through the lower accretionary complex ( $P_{lac}$ ) as well as the reflections from the upper plate and the downgoing oceanic slab (*cf.* Figs 11 and 12) could be generated using a velocity–depth model that corresponds to the model derived from forward ray tracing shown in Fig. 5. As the minor inclination of the seafloor and the structural layers in the model for profile 02 as well as the lateral thickness variations of the sedimentary layers of profile 03 cannot be accounted for in the 1-D calculations, some discrepancies in the traveltimes of the real and synthetic data must be expected. If amplitude variations with offset within each phase of the real data are due to 2-D and 3-D ray focusing and defocusing effects, they cannot be reproduced with the reflectivity method. Focusing effects are documented along both profiles. For example, the  $P_{up}P$  refraction recorded by OBH 20 shows a significant amplitude decrease around profile distance 95 km, before higher amplitudes are observed again at approximately 100 km profile distance. The same amplitude pattern is observed on OBH 17 (Fig. 12) and OBH 19 (not shown). Similar focusing and defocusing effects influence the phase  $P_{lac}$  of OBH 32 (Fig. 11), for which the observed amplitude undulations occur at approximately identical profile distances for neighbouring stations. The main targets of this synthetic modelling, however, are the reflections from the upper plate and the subducted oceanic plate ( $P_{up}P$  and  $P_{loc}$ , respectively), for which adequate amplitude characteristics could be achieved. On OBH 32, reflection amplitudes from the leading edge of the upper plate increase from 20 km offset, whereas significant amplitudes from the reflection  $P_{loc}$  appear at offsets of around 32 km. The general amplitude decrease of several phases beyond 37 km offset is again due to defocusing effects, as this lack of reflectivity is observed on several stations along this profile. OBH 20 records the subducted plate beneath the forearc basin at approximately 21 km depth (Fig. 17). The amplitudes from the corresponding onset arrive at late times and are strongest at offsets greater than 60 km. This amplitude pattern is also confirmed in the synthetic data. The velocity–depth profile used for the dynamic modelling is shown for both stations in Fig. 17. The grey-shaded area signifies the subducted plate. Minor revisions compared to the velocity field derived from forward modelling have been adopted,

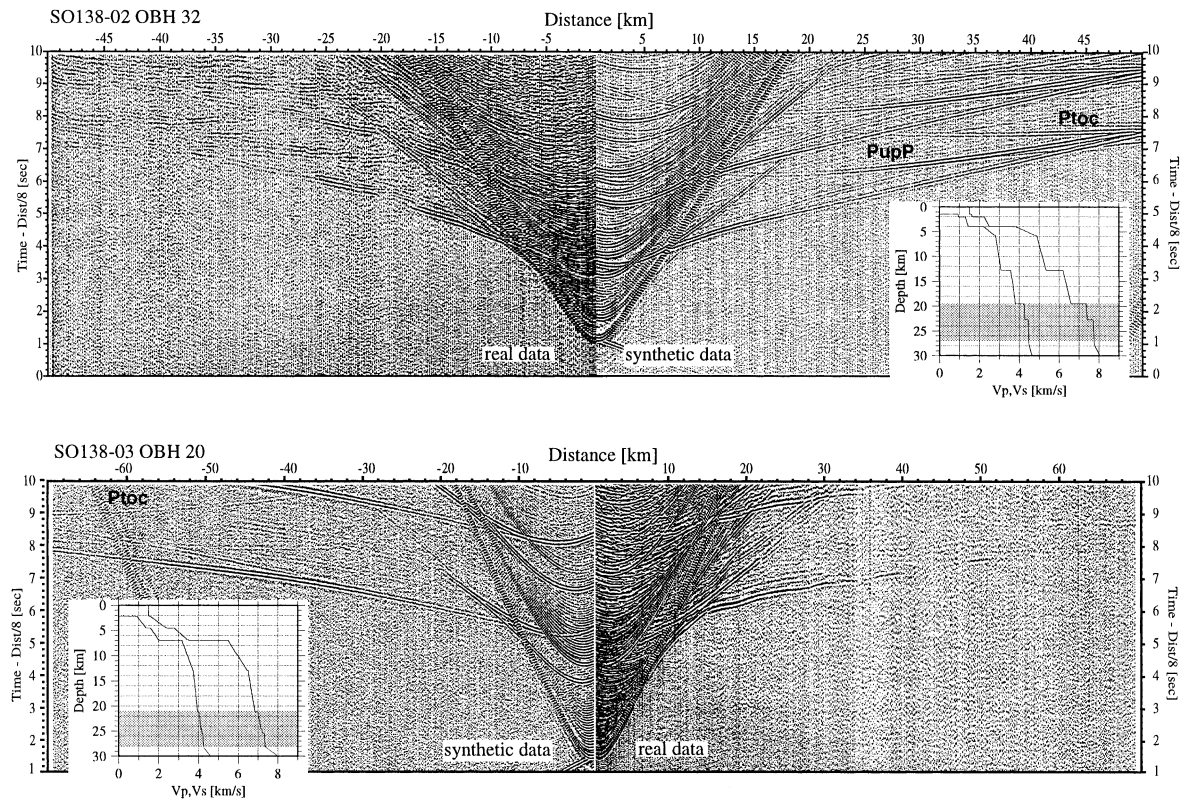


**Figure 17.** 1-D synthetic data modelling conducted for two stations deployed along strike-lines SO138-02 and SO138-03 to verify phases recorded from the leading edge of the upper plate ( $P_{up}P$ ) and the top of the subducted plate ( $P_{loc}$ ). The dynamic modelling procedure employs the reflectivity method and is based on the velocity models derived from kinematic forward modelling (Figs 11 and 12). The synthetic seismograms are filtered with identical parameters to those used for the real data to ensure compatibility. In the  $P$ - and  $S$ -wave velocity–depth profiles, the depth range of the subducted plate is shaded grey.

but the overall velocity–depth structure is consistent with the results presented in Fig. 5.

## 5.2 Structure of the accretionary domain and outer high

Along both dip-lines an active accretionary domain is identified consisting of the material above the subducting slab bordered laterally by the deformation front and the slope break, which is the surface expression of an underlying backstop structure (Figs 3a and 4a). Several smaller ridges are the geomorphological indication of active accretion of the trench-fill sediment, which causes partial stacking and folding between the deformation front and the slope break. Imbricate thrust faulting is recognized on both lines. Whereas the Sumatra transect displays a chaotic seismic signature of the active accretionary domain, the internal structure along the Sunda Strait segment is not completely destroyed, although it is highly deformed. One possible explanation for this might be found in the stress pattern of the Sumatran sector, which will be influenced by the strain partitioning occurring here due to the oblique component of subduction. The forearc region off Sumatra bounded seawards by the trench is experiencing arc-parallel stretching, which may influence the destruction of stratigraphic layering.

Active accretion is also supported by the velocity model (Figs 5 and 6). Laterally increasing velocities are characteristic of the frontal prism up to the location of the backstop structure. The low seismic velocities are representative of young accreted sediment. On both lines, the backstop structure marks the transition from the active accretionary domain to the outer

high and cuts the entire accretionary units to near the top of the subducted plate. Landwards, tectonic activity is still evident in a number of thrusts on the outer high, but is greatly reduced compared to the active accretionary domain. The reflectivity of the outer high along both reflection lines is limited. On line SO137-12 the rough basement top, which appears landwards of the outer high crest (Fig. 3b), further inhibits the reflectivity of the lower segments. A similar basement top is present on the Sunda Strait line, although more internal structure within the basement is resolved that displays a chaotic pattern of thrusting and possible rotation of entire blocks. Velocities show laterally constant values within the outer high, solely increasing with depth due to the greater overburden and material compaction. In view of the large dimensions of the outer high and its great depth, velocities are fairly low ( $<5.8 \text{ km s}^{-1}$  off southern Sumatra and  $<5.2 \text{ km s}^{-1}$  off the Sunda Strait at approximately 15 km depth). This velocity structure is indicative of a sedimentary composition, possibly including metamorphosed material near the base. The density values used in the gravity modelling for the dip-lines and that correlate with the seismic velocities and structural model are typical of compacted sedimentary material.

## 5.3 Forearc domain

The most striking difference between the two transects concerns the crustal structure of the forearc domain and the corresponding lack of a morphological basin off the Sunda Strait. In contrast, the forearc basin off southern Sumatra lies at 2200 m

seafloor depth. It has a lateral width of over 80 km and is bounded by the Sumatra shelf to the northeast (Fig. 3c). The seaward part of the basin is highly affected by the presence of the Mentawai fault anticlinal structure, causing a significant uplift of the seafloor. The Mentawai fault separates the main basin from a smaller sub-basin, which carries less sediment infill. We interpret this segment between CDPs 16 800 and 18 700 as forming part of the forearc basin complex as the basement top beneath the forearc basin sedimentary fill continues to below the sub-basin (Figs 3b and c). Nonetheless, the Mentawai fault poses a structural break there and is possibly related to the uplift of the sub-basin with respect to the main forearc basin.

The lack of an analogous morphological basin off the Sunda Strait correlates with the locally concave shape of the trench and deformation front there, resulting from the northwestward motion of the Sumatra sliver plate, for which the area off the Sunda Strait acts as a trailing edge (Huchon & Le Pichon 1984). Thus the influence of strain partitioning due to the oblique subduction component off Sumatra is manifested in the morphology of the Sunda Strait transect, but leaves no indication in the forearc morphology off southern Sumatra. The forearc domain along the Sunda Strait line (CDPs 13 100–17 900 in Fig. 4c) shows a comparable lateral width and sediment accumulation. In contrast to line 12, the sediment there is highly deformed. The intense folding and partial stacking mainly affects the older sequences; the younger units are not as strongly altered. The presence of a strong BSR observed in the forearc domain along both lines indicates the lower boundary of the gas hydrate stability zone. Unlike most other known occurrences of gas hydrates worldwide, the distribution of gas hydrate and free gas at the central Sunda margin is limited to the forearc domain. The absence of a BSR along the accretionary domain and outer high is probably due to the intense active faulting observed there (Figs 3a, 3b, 4a and 4b), which potentially allows the escape of free gas.

Both forearc domains carry a several kilometre thick sedimentary infill (over 4 km on the Sunda Strait transect and over 4.5 km off southern Sumatra). Seismic stratigraphy investigations of the forearc basin north of Nias island (Beaudry & Moore 1981, 1985; Izart *et al.* 1994) were correlated with bore-hole information and indicate a Neogene history characterized by subsidence and continuous sedimentation. Thus the sedimentary sequences overlying the Palaeogene basement are of Miocene age and were deposited after a late Oligocene initiation or rejuvenation of subduction along the margin, leading to uplift of the subduction complex. Off southern Sumatra, the seaward-dipping basement top is a layer with velocities ranging from 5.3 to 5.7 km s<sup>-1</sup> (Fig. 5) and with increasing thickness from 1.5 km beneath the shelf to 4 km beneath the seaward part of the basin. Beneath this layer, velocities increase from 6.0 to over 6.5 km s<sup>-1</sup> within the leading edge of the upper plate. These velocity values correspond roughly to results from earlier refraction studies conducted around Nias island (Kieckhefer *et al.* 1980). The velocity structure observed within the leading edge of the upper plate (thin black line in Fig. 18) closely matches the results compiled by Christensen & Mooney (1995) (thick grey line in Fig. 18) for an average continental crustal model including continental arcs.

Off the Sunda Strait, a different situation emerges as velocities beneath the basement top range from 3.9 to 5.2 km s<sup>-1</sup> within a 6.5–8.5 km thick unit beneath the forearc domain (Fig. 6). These velocities are identical to the velocity structure found

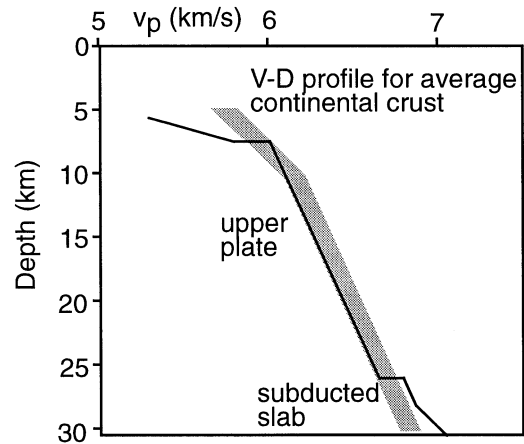


**Figure 18.** Comparison between a representative velocity–depth profile from the forearc domain of line SO138-01 (thin black line) and a two-gradient average continental crust model (thick grey line) after Christensen & Mooney (1995). The velocities found beneath the Sumatran forearc basin, although towards the lower end of the range of average values, are indicative of continental-type crust.

beneath the outer high, whereas off Sumatra a significant velocity increase was found. At greater depth, velocities ranging from 6.0 to over 6.5 km s<sup>-1</sup> correspond to the Sumatran results. Further landwards, beneath the Java shelf, a substantial velocity increase is observed. Velocities of 4.3 km s<sup>-1</sup> at 2 km depth correspond to values reported by Legemann *et al.* (2000) for a basement ridge at the southwestern entrance to the Sunda Strait. The high gravity values of over 80 mgal observed here also indicate a shallow basement. Further north along the central segment of the Sunda Strait, the ridge is broken into several basement blocks that mark the eastern boundary of the Sunda Strait transtensional basin. This basin or graben formed in conjunction with the northwestward motion of the Sumatra sliver plate (Legemann *et al.* 2000).

## 6 SUMMARY AND CONCLUSIONS

An integrative analysis of wide-angle and near-vertical-incidence reflection seismic data provides new insights into the structure of the subduction complex off southern Sumatra and Sunda Strait. Additional 2-D gravity modelling and synthetic seismic data further constrain the following results.

(1) The configuration of the descending slab is determined along both transects by the MCS and OBH data for the upper 20 km. Near the deformation front, the plate dips gently at about 3° off Sumatra and at 4° off the Sunda Strait. Beneath the outer high and the forearc domain, late arrivals from the plate boundary and from the oceanic Moho are identified in the wide-angle data and show a dip gradually increasing to 5° off Sumatra and 7° off the Sunda Strait, respectively. The lateral increase in the plate dip to the southeast is supported by the gravity modelling conducted along the dip-lines. The Sumatran results are further supported by reflections observed on strike-lines SO138-02 and SO138-03, which track the subducted plate at 19 and at 21–22 km depth, respectively. These 3-D constraints could successfully be modelled with synthetic data.

(2) Along both transects an active accretionary prism occupies the frontal part of the subduction complex and is separated from the outer high by a backstop structure. This accretionary



domain is characterized by the generation of accretionary ridges and by intense tectonic activity resulting in numerous faults. Seismic velocities show a lateral positive gradient landwards and values typical of young accreted sediment.

(3) The extensive outer high domain shows comparable lateral dimensions of 85–90 km along both dip-lines. Off Sumatra, the leading edge of the upper plate is found at over 16 km depth, whereas off the Sunda Strait a shallower upper plate transition (13 km) is consistent with the velocity structure observed there. The rugged seafloor topography and underlying rough basement top of the outer high on both profiles inhibit the reflectivity, and little internal structure is resolved. The loss in resolution suggests a higher degree of deformation and compaction of the underlying material, also indicated by the velocity structure of the outer high. Seismic velocities derived from the wide-angle data are moderate along both transects, indicating a possible sedimentary composition. Metamorphosed material may be present at the base, but in view of the modest velocity values, an overall igneous or ophiolitic composition seems unlikely. Tectonic activity is evident from faults on both sections and ongoing deformation of the ponded sediment in the basins created by the rough basement top is expressed in the ridge and trough morphology.

(4) The main difference between the two transects is in the nature of the lower forearc domain and the absence of a distinct forearc basin off the Sunda Strait. A typical discrete basin is only observed off southern Sumatra, forming part of a chain of forearc basins along the margin. The velocity structure beneath the basin indicates a continental-type crust forming the forearc basement. Several kilometres of sediment fill record the Miocene to Quaternary depositional history of the basin. A similar amount of sediment is found off Sunda Strait, where the clear-cut onset of the Java shelf represents the transition to the morphological features within Sunda Strait. These morphological features are related to the transtensional evolution of the Sunda Strait pull-apart basin. The nature of the forearc basement off Sunda Strait remains unclear, as seismic velocities here are lower than off Sumatra.

## ACKNOWLEDGMENTS

We are grateful to Cpt. Papenhagen and the crew of RV *Sonne* for their assistance at sea during the GINCO cruises. Many thanks go to all cruise participants for their help with data acquisition and processing. We also thank C. Kopp for support during modelling and data analysis and C. Ranero and R. von Huene for many discussions during the early stage of this work. Reviews by two anonymous referees are greatly appreciated. We used the GMT software (Wessel & Smith 1991) for several figures. The GINCO project is supported by the German Federal Ministry for Science and Technology (BMBF).

## REFERENCES

- Barton, P.J., 1986. The relationship between seismic velocity and density in the continental crust, a useful constraint?, *Geophys. J. R. astr. Soc.*, **87**, 195–208.
- Beaudry, D. & Moore, G., 1981. Seismic-stratigraphic framework of the forearc basin off central Sumatra, Sunda Arc, *Earth planet. Sci. Lett.*, **54**, 17–28.
- Beaudry, D. & Moore, G., 1985. Seismic stratigraphy and Cenozoic evolution of West Sumatra forearc basin, *Am. Assoc. Petrol. Geol. Bull.*, **69**, 742–759.
- Bellier, O. & Sébrier, M., 1995. Is the slip rate variation on the Great Sumatran Fault accommodated by fore-arc stretching?, *Geophys. Res. Lett.*, **22**, 1969–1972.
- Carlson, R.L. & Raskin, G.S., 1984. Density of the ocean crust, *Nature*, **311**, 555–558.
- Christensen, N.I. & Mooney, W.D., 1995. Seismic velocity structure and composition of the continental crust: a global view, *J. geophys. Res.*, **100**, 9761–9788.
- Curry, J.R., Shor, G.G., Raitt, R.W. & Henry, M., 1977. Seismic refraction and reflection studies of crustal structure of the eastern Sunda and western Banda Arcs, *J. geophys. Res.*, **82**, 2479–2489.
- DeMets, C., Gordon, R.G., Argus, D.F. & Stein, S., 1990. Current plate motions, *Geophys. J. Int.*, **101**, 425–478.
- DeMets, C., Gordon, R.G., Argus, D.F. & Stein, S., 1994. Effects of recent revisions to the geomagnetic reversal time scale on estimates of current plate motions, *Geophys. Res. Lett.*, **21**, 2191–2194.
- Diamant, M., Deplus, C., Harjono, H., Larue, M., Lassal, O., Dubois, J. & Renard, V., 1990. Extension in the Sunda Strait (Indonesia): a review of the Krakatau programme, *Oceanologica Acta Spec. Vol.*, **10**, 31–42.
- Diamant, M. *et al.*, 1992. Mentawai fault zone off Sumatra: a new key to the geodynamics of western Indonesia, *Geology*, **20**, 259–262.
- Fitch, T.J., 1972. Plate convergence, transcurrent faults and internal deformation adjacent to southeast Asia and the western Pacific, *J. geophys. Res.*, **77**, 4432–4460.
- Flueh, E.R. & Bialas, J., 1996. A digital, high data capacity ocean bottom recorder for seismic investigations, *Int. Underwater Syst. Design*, **18**, 18–20.
- Flueh, E.R. *et al.*, 1999. GINCO2 (SONNE Cruise SO-138): geoscientific investigations along the active convergence zone between the Eastern Eurasian and Indo-Australian Plates off Indonesia, *Cruise Report*, Geomar, Kiel.
- Hamilton, W., 1979. Tectonics of the Indonesian region, *USGS Prof. Pap.*, **1078**.
- Hamilton, W., 1988. Plate tectonics and island arcs, *Geol. Soc. Am. Bull.*, **100**, 1503–1527.
- Harjono, H., 1991. Seismicity of the Sunda Strait: evidence for crustal extension and volcanological implications, *Tectonics*, **10**, 17–30.
- Heyde, I., Roeser, H.A. & Schreckenberger, B., 2000. Gravimetric measurements and their interpretation, *GINCO Final Rept*, Part I, BGR, Hannover.
- Huchon, P. & Le Pichon, X., 1984. Sunda Strait and Central Sumatra fault, *Geology*, **12**, 668–672.
- Izart, A., Mustafa Kemal, B. & Malod, J.A., 1994. Seismic stratigraphy and subsidence evolution of the northwest Sumatra fore-arc basin, *Mar. Geol.*, **122**, 109–124.
- Kieckhefer, R.M., Shor, G.G., Jr & Curry, J.R., 1980. Seismic refraction studies of the Sunda trench and forearc basin, *J. geophys. Res.*, **85** (B2), 863–889.
- Legemann, H., Gutscher, M.-A., Bialas, J., Flueh, E.R., Weinrebe, W. & Reichert, C., 2000. Transtensional basins in the western Sunda Strait, *Geophys. Res. Lett.*, **27**, 3545–3548.
- Ludwig, W.J., Nafe, J.E. & Drake, C.L., 1970. Seismic refraction, in *The Sea*, Vol. 4, pp. 53–84, ed. Maxwell, A.E., Interscience, New York.
- Luetgert, J., 1992. MacRay-Interactive two-dimensional seismic ray-tracing for the Macintosh, *USGS Open File Rept*, **92-356**.
- Malod, J.A., Karta, K., Beslier, M.O. & Zen, M.T., Jr, 1995. From normal to oblique subduction: tectonic relationships between Java and Sumatra, *J. SE Asian Earth Sci.*, **12**, 85–93.
- Malod, J.A. & Kemal, B.M., 1996. The Sumatra margin: oblique subduction and lateral displacement of the accretionary prism, in *Tectonic Evolution of Southeast Asia*, eds Hall, R. & Blundell, D., *Geol. Soc. Spec. Publ.*, **106**, 19–28.

- McCaffrey, R., 1991. Slip vectors and stretching of the Sumatran forearc, *Geology*, **19**, 881–884.
- McCaffrey, R., 1992. Oblique plate convergence, slip vectors, and forearc deformation, *J. geophys. Res.*, **97** (B6), 8905–8915.
- McCaffrey, R., 1996. Slip partitioning at convergent plate boundaries of SE Asia, in *Tectonic Evolution of Southeast Asia*, eds Hall, R. & Blundell, D., *Geol. Soc. Spec. Publ.*, **106**, 3–18.
- Moore, G.F., Curray, J.R., Moore, D.G. & Karig, D.E., 1980. Variations in geologic structure along the Sunda fore arc, Northeastern Indian Ocean, in *The Tectonic and Geologic Evolution of Southeast Asian Seas and Islands*, ed. Hayes, D., *Geophys. Monogr.*, **23**, 145–160.
- Prawirodirdjo, L. *et al.*, 1997. Geodetic observations of interseismic strain segmentation at the Sumatran subduction zone, *Geophys. Res. Lett.*, **24**, 2601–2604.
- Puspito, N.T. & Shimazaki, K., 1995. Mantle structure and seismotectonics of the Sunda and Banda arcs, *Tectonophysics*, **251**, 215–228.
- Reichert, C. *et al.*, 1999. GINCO1 (SONNE Cruise SO-137): geoscientific investigations along the active convergence zone between the Eastern Eurasian and Indo-Australian Plates off Indonesia, *Cruise Rept*, BGR, Hannover.
- Samuel, M.A. & Harbury, N.A., 1996. The Mentawai fault zone and deformation of the Sumatran forearc in the Nias area, in *Tectonic Evolution of Southeast Asia*, eds Hall, R. & Blundell, D., *Geol. Soc. Spec. Publ.*, **106**, 337–351.
- Samuel, M.A., Harbury, N.A., Jones, M.E. & Matthews, S.J., 1995. Inversion-controlled uplift of an outer-arc ridge: Nias Island, offshore Sumatra, in *Basin Inversion*, eds Buchanan, J.G. & Buchanan, P.G., *Geol. Soc. Spec. Publ.*, **88**, 473–492.
- Sandwell, D.T. & Smith, W.H.F., 1997. Marine gravity anomaly from Geosat and ERS1 satellite altimetry, *J. geophys. Res.*, **102** (B5), 10 039–10 054.
- Tregoning, P. *et al.*, 1994. First geodetic measurement of convergence across the Java Trench, *Geophys. Res. Lett.*, **21**, 2135–2138.
- Wessel, P. & Smith, W.H.F., 1991. Free software helps map and display data, *EOS, Trans. Am. geophys. Un.*, **72**, 445–446.
- White, R.S., McKenzie, D. & O’Nions, R.K., 1992. Oceanic crustal thickness from seismic measurements and rare earth element inversions, *J. geophys. Res.*, **97** (B13), 19 681–19 715.
- Widiyantoro, S. & van der Hilst, R., 1996. Structure and evolution of lithospheric slab beneath the Sunda Arc, Indonesia, *Science*, **271**, 1566–1570.